Chapter 4

Dynamics of $O(^3P)$ + CO_2 collisions at hyperthermal energies

In collaboration with Mitchio Okumura, Jianming Zhang, Timothy K. Minton, Jeffrey T. Paci, Jan M. L. Martin, Jon M. Camden, and George C. Schatz; parts of this will be submitted to *Journal of Physical Chemistry A* for publication.

4.1 Abstract

The dynamics of $O(^3P) + CO_2$ collisions at hyperthermal collision energies near 100 kcal mol^{-1} were investigated experimentally and theoretically. Crossed-molecular-beam experiments at $\langle E_{\text{coll}} \rangle = 98.8$ kcal mol^{-1} were performed with isotopically labeled $^{12}C^{18}O_2$ to distinguish products of non-reactive scattering [$^{16}O(^3P) + {}^{12}C^{18}O_2$] from products of reactive scattering ($^{18}O + {}^{16}O^{12}C^{18}O$ and $^{18}O^{16}O + {}^{12}C^{18}O$). ^{16}O products were detected mainly in the forward direction, i.e., in the initial direction of the hyperthermal oxygen beam in the center-of-mass (c.m.) frame, and they contained ~87% of the collision energy in translation, on average; the amount of energy transfer during non-reactive scattering depended on impact parameter. $^{16}O^{12}C^{18}O$ products from the oxygen isotope exchange reaction were scattered mainly in the backward direction with 35% of the available energy in translation, on average. $^{18}O^{16}O$ products from the oxygen-atom abstraction reaction were detected in the forward direction, with 56% of the available energy in translation, on average. Stationary points on the lowest triplet potential energy surface of the $O(^3P) + CO_2$ system were characterized at the CCSD(T)/aug-cc-pVTZ level of theory. Quasi-classical trajectory (QCT) calculations of $O(^3P) + CO_2$ collisions at energies between 1.0 – 6.5 eV (23 – 150 kcal mol^{-1}) were performed at the B3LYP/6-311G(d) and BMK/6-311G(d) levels of theory, and both reactive channels observed in the experiment were also predicted by the theory. In addition, trajectories leading to the formation of $^{18}O_2 + {}^{12}C^{16}O$ products were predicted. The c.m. translational energy and angular distributions derived from the QCT calculations show qualitative, but not quantitative agreement with experimental results. The theoretical relative product yield for the oxygen isotope exchange reaction also agreed well with the experiment. The isotope exchange reaction demonstrates a new pathway through which oxygen isotopes may be cycled in the upper atmosphere, where $O(^3P)$ atoms with hyperthermal translational energy distributions can be generated through the photolysis of ozone and molecular oxygen.

4.2 Introduction

Atomic oxygen radicals in the atmosphere play an important role in regulating Earth's oxidative and radiative balance. Photodissociation of molecular oxygen and ozone by solar ultraviolet radiation produces not only electronically excited $O(^1D)$ and $O(^1S)$, but also ground-state $O(^3P)$ with velocities as high as 6 km s^{-1} [*Matsumi and Kawasaki*, 2003; *Stranges et al.*, 1995]. $O(^3P)$ has received less attention than $O(^1D)$ and $O(^1S)$, however, because it is less reactive at low collision energies. Yet, its important role in the terrestrial mesosphere and thermosphere is widely recognized; for instance, its collisions with CO_2 significantly influence the population of $CO_2(010)$, whose emission at 15 μm cools the atmosphere and regulates the height of the mesopause [*Sharma and Roble*, 2002]. $O(^3P)$ can also interact with CO_2 from space vehicle exhaust streams at relative velocities near 8 km s^{-1} and collision energies near 100 kcal mol^{-1}, well above those expected at local thermodynamic equilibrium.

These high collision energies exceed barriers to (*1*) CO_3 formation, leading to oxygen isotope exchange, and (*2*) oxygen-atom abstraction on the triplet potential energy surface (PES) [*Averyanov et al.*, 1999; *Bennett et al.*, 2004; *Froese and Goddard*, 1993; *Mebel et al.*, 2004; *Yang et al.*, 2005]. The enthalpies associated with these reactions are:

$$O(^3P) + CO_2(^1\Sigma_g^+) \rightarrow O(^3P) + CO_2(^1\Sigma_g^+) \qquad \Delta H \sim 0 \qquad (4.1)$$

$$\rightarrow O_2(^3\Sigma_g^-) + CO(^1\Sigma^+) \qquad \Delta H = 8\ \text{kcal mol}^{-1} \qquad (4.2)$$

A reaction analogous to reaction 4.1, between $O(^1D)$ and CO_2 in the stratosphere [*Baulch and Breckenridge*, 1966; *Chakraborty and Bhattacharya*, 2003; *DeMore and Dede*, 1970; *Johnston et al.*, 2000; *Mebel et al.*, 2004; *Perri et al.*, 2003, 2004; *Shaheen et al.*, 2007; *Wen and Thiemens*, 1993; *Yeung et al.*, 2009a], alters the stable isotope composition of stratospheric CO_2, allowing the isotopic composition of stratospheric CO_2 to be used as a tracer of $O(^1D)$ [*Thiemens et al.*, 1995; *Yung et al.*, 1991, 1997] and atmospheric transport [*Boering et al.*, 2004]. The isotopic composition of CO_2 has also been proposed as a tracer of biogeochemical cycles on annual and decadal timescales [*Hoag et al.*, 2005]. Consequently, the dynamics of reactive channels that could alter the isotopic composition of upper atmospheric CO_2 are also of interest [*Perri et al.*, 2003, 2004].

Early studies on the $O(^3P)$ + CO_2 system were primarily theoretical and focused on the vibrational-state-specific energy transfer [*Bass*, 1974; *Garrett*, 1983; *Harvey*, 1982; *Schatz and Redmon*, 1981]. The mechanism was found to be primarily impulsive at high collision energies, like that of collisions between CO_2 and noble gases [*Billing and Clary*, 1983; *Harvey*, 1982; *Schatz and Redmon*, 1981]. More recent quantum calculations on the $O(^3P_J)$ + $CO_2(010)$ system indicate that vibrational-to-translational energy transfer is sensitive to the total angular momentum J at thermal collision energies, although the importance of spin-orbit coupling decreases with increasing collision energy [*de Lara-Castells et al.*, 2006, 2007]. Two experimental studies also focused on state-specific excitation in $O(^3P)$ + CO_2 collisions, specifically to $CO_2(001)$; both studies also reported evidence that reaction 4.2, which is important in combustion chemistry [*Tsang and Hampson*, 1986] yielded vibrationally excited CO products [*Oakes et al.*, 1994; *Upschulte and Caledonia*, 1992]; no mechanism was proposed, however.

We recently confirmed the presence of reaction 4.1 at hyperthermal collision energies [*Yeung et al.*, 2009b], and we intend now to investigate its dynamics. *Mebel et al.* [2004] suggested that the dynamics of CO_3 formation on the triplet ($^3A'$) PES with hyperthermal $O(^3P)$ atoms might be complicated by a nearby $^3A'$–$^1A'$ intersection seam, which could lead to non-adiabatic effects along reactive trajectories. Indeed, many low-lying electronic states of CO_3 (e.g., $^3A''$) lie within several eV of $CO_3(^3A')$, so vibronic [*Kowalczyk and Krylov*, 2007] and/or spin-orbit [*Mebel et al.*, 2004] coupling could result in unexpected curvature and dynamics on the triplet PES.

Here, the results of theoretical and crossed-molecular-beam studies of $O(^3P)$ + CO_2 collisions at hyperthermal collision energies will be presented. Theoretical direct dynamics calculations using the QCT method on an adiabatic PES were compared with the results from an experimental dynamics study obtained for an average collision energy $\langle E_{\rm coll}\rangle = 98.8$ kcal mol^{-1}. The oxygen isotope exchange and oxygen-atom abstraction reactions were observed in both the QCT calculations and the laboratory experiment, and center-of-mass (c.m.) angular and translational energy distributions for the oxygen isotope exchange reaction were obtained. Their implications for atomic oxygen cycling through CO_2 in the atmosphere will be discussed.

4.3 Theoretical studies

4.3.1 Electronic structure calculations

Geometry-optimization, single-point, and vibrational-frequency calculations were performed on stationary points of the lowest triplet PES of CO_3, $^3A''$; a discussion of the relative energetics of the $^3A'$ and $^3A''$ surfaces can be found in Section 4.5. Stationary points for reactions 4.1 and 4.2 were characterized using electronic structure calculations at the B3LYP/6-311G(d) [*Becke*, 1993; *Frisch et al.*, 1984; *Lee et al.*, 1988], BMK/6-311G(d) [*Boese and Martin*, 2004], and CCSD(T)/aug-cc-pVTZ [*Kendall et al.*, 1992; *Raghavachari et al.*, 1989] levels of theory/basis using the MOLPRO electronic structure code [*Werner et al.*, 2006]. Confirmation of transition-state character was achieved by inspection of the associated vibrational frequencies. Other reactive channels were not characterized because reactant energies in excess of 250 kcal mol^{-1} are required to open them, according to our B3LYP/6-311G(d) calculations.

Here, we report three transition-state structures and one bound-state structure on the $CO_3(^3A'')$ PES; the results are shown in Figures 4.1 and 4.2 and Table 4.1 [*Mebel et al.*, 2004]. All structures are planar. One transition state (TS1) and the bound state (CO_3) were associated with the $O(^3P) + CO_2$ isotope exchange reaction. Two transition states (TS2 and TS3) were associated with the oxygen-atom abstraction reaction producing O_2 and CO. Two additional bound states and two associated transition states were also found; they resemble the C_s minima reported in previous work [*Bennett et al.*, 2004; *Froese and Goddard*, 1993; *Mebel et al.*, 2004], but they will not be discussed here because neither of the bound states were bound when zero-point energy (ZPE) was considered. For this reason, we are also not reporting minima in the van der Waals region of the PES, e.g., the quadrupole-induced minimum ($\Delta E \sim 335$ cm^{-1}) at the RCCSD(T)/aug-cc-pVTZ level of theory [*de Lara-Castells et al.*, 2006, 2007], because the binding energies were below the ZPE of the system. Further

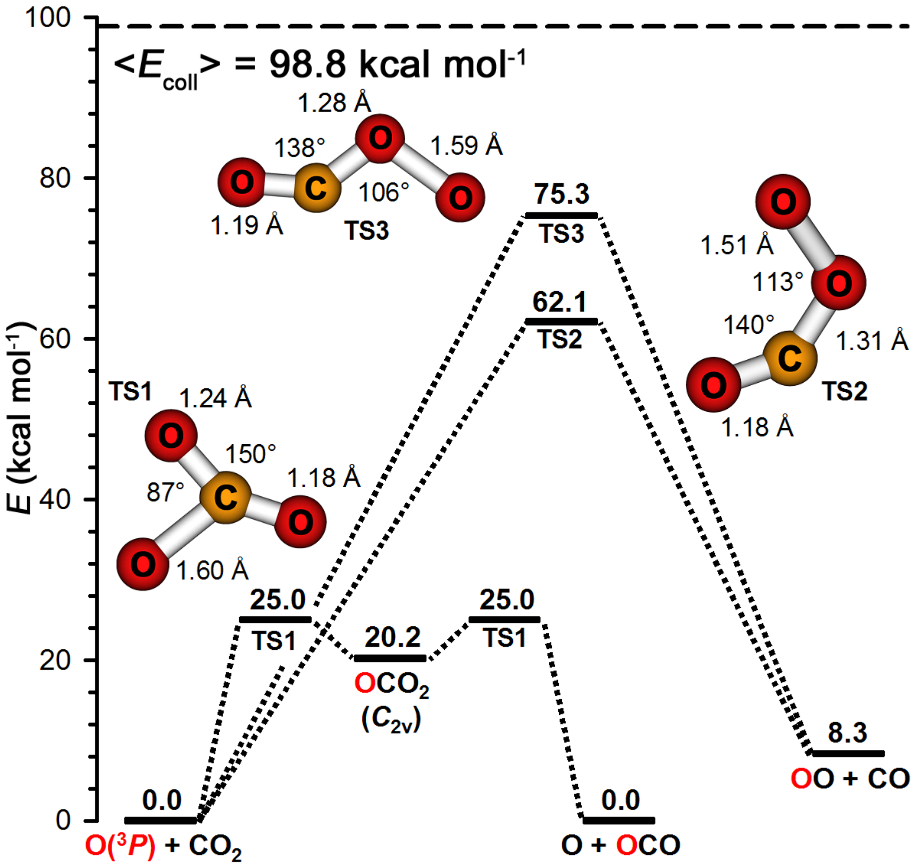

Figure 4.1: **Stationary-point structures for O(^3P) + CO_2 reactions below 100 kcal mol^{-1} calculated at the CCSD(T)/aug-cc-pVTZ level of theory on the $^3A''$.** The relative energies have been corrected for zero-point energy.

comparisons of the structures with previous work on the lowest triplet PES will be presented in Section 4.5.

Of the levels of theory and basis examined in this study, CCSD(T)/aug-cc-pVTZ is probably the most accurate combination; however, multi-reference character in the stationary points may be important because several electronic surfaces are within several eV of the PES that is the subject of this study [*Bennett et al.*, 2004; *Kowalczyk and Krylov*, 2007; *Mebel et al.*, 2004]. Multi-reference CCSD(T) calculations, unfortunately, were not computationally affordable. Still, our CCSD(T)/aug-cc-pVTZ geometries are nearly identical to those obtained in recent calculations using the W4 method [*Karton et al.*, 2006] near the full-configuration-interaction and complete-basis-set limits, with transition-state energies within 2 kcal mol^{-1} and the bound-state energy within 4 kcal mol^{-1} (J. M. L. Martin, per-

Table 4.1: Energies (kcal mol^{-1}) for the stationary points on the lowest triplet CO_3 potential energy surface for $^{16}O(^3P) + ^{12}C^{16}O_2 \rightarrow ^{16}O + ^{12}C^{16}O_2$ collisions

	B3LYP 6-311G(d)		**BMK 6-311G(d)**		**CCSD(T) aug-cc-pVTZ**		**CCSD(T) 6-311+G(3df)***
		w/ZPEC†		w/ZPEC†		w/ZPEC†	
$O(^3P) + CO_2$	0.0	0.0	0.0	0.0	0.0	0.0	0.0
TS1	18.0	17.7	25.2	25.0	25.2	25.0	35.2
CO_3	11.8	11.3	20.2	19.0	21.8	20.2	22.0
TS2	56.2	55.2	65.3	64.5	63.0	62.1	
TS3	70.3	69.2	80.0	78.9	76.5	75.3	
$O_2 + CO$	9.7	7.9	14.3	12.6	10.2	8.3	

*From *Mebel et al.* [2004] using a $^3A'$ geometry optimized at the CASSCF(16,13)/6-311G(d) level of theory. The authors noted that the more ideal MRCI+Q/6-311+G(3df) energy calculation was not affordable.

†Zero-point-energy correction (ZPEC).

sonal communication). Thus, we used the CCSD(T)/aug-cc-pVTZ geometries and energies as benchmarks for comparison with those calculated by the density-functional methods, which are more affordable for QCT calculations.

In addition to using the B3LYP and BMK levels of theory, we characterized the transition-state structures at the MP2 [*Møller and Plesset*, 1934], M06-2X [*Zhao and Truhlar*, 2008], and CCSD [*Purvis and Bartlett*, 1982] levels using the 6-31G(d,p), 6-311G(d), and cc-pVTZ [*Dunning*, 1989] basis sets during our search for an appropriate level of theory for QCT calculations (optimizing computational cost and accuracy). The density-functional methods B3LYP/6-311G(d) and BMK/6-311G(d), however, were found to have the best balance between computational cost and accuracy, so we will only report the results of those calculations here along with the results of CCSD(T)/aug-cc-pVTZ calculations (see Figure 4.2). The results of the lower-level B3LYP and BMK calculations, along with the MP2, M06-2X, and CCSD calculations, are shown in Figure 4.3.

TS1 had C_s symmetry in all cases. Mild compression of one C–O bond and stretching of the other C–O bond in the parent CO_2, along with moderate bending (~30°) of the O–C–O bond angle, was found at all levels of theory. The geometries were similar to that calculated at the CCSD(T) level of theory, which had C–O bond lengths of 1.24 Å, 1.18 Å, and 1.60 Å and bond angles of 87°, 123°, and 150° (see Figure 4.2). The B3LYP geometry

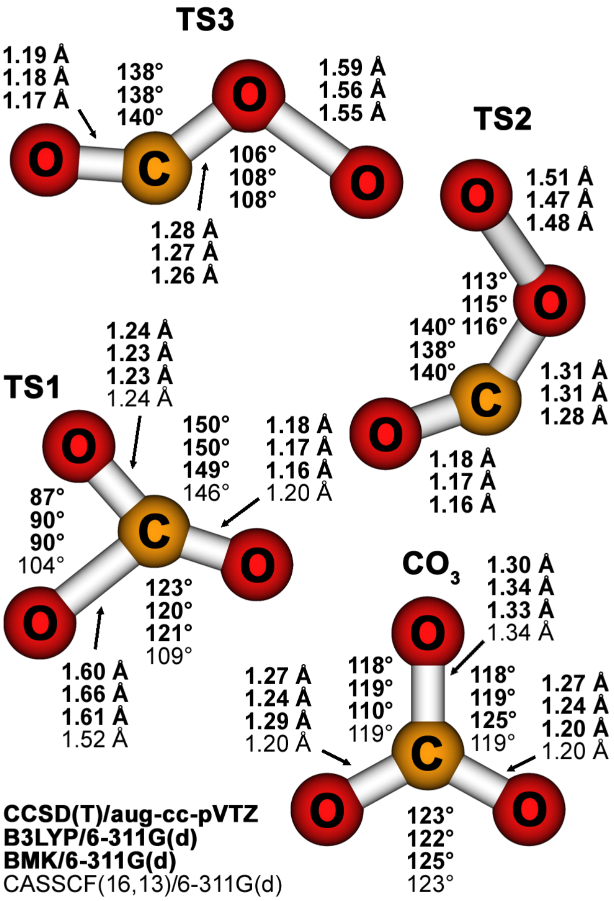

Figure 4.2: **Comparison of CO_3 stationary point geometries relevant to the QCT calculations.** Our geometry optimizations at the CCSD(T)/aug-cc-pVTZ, B3LYP/6-311G(d), and BMK/6-311G(d) levels of theory (bold) are shown with *Mebel et al.*'s CASSCF(16,13)/6-311G(d) geometries for CO_3 and TS1.

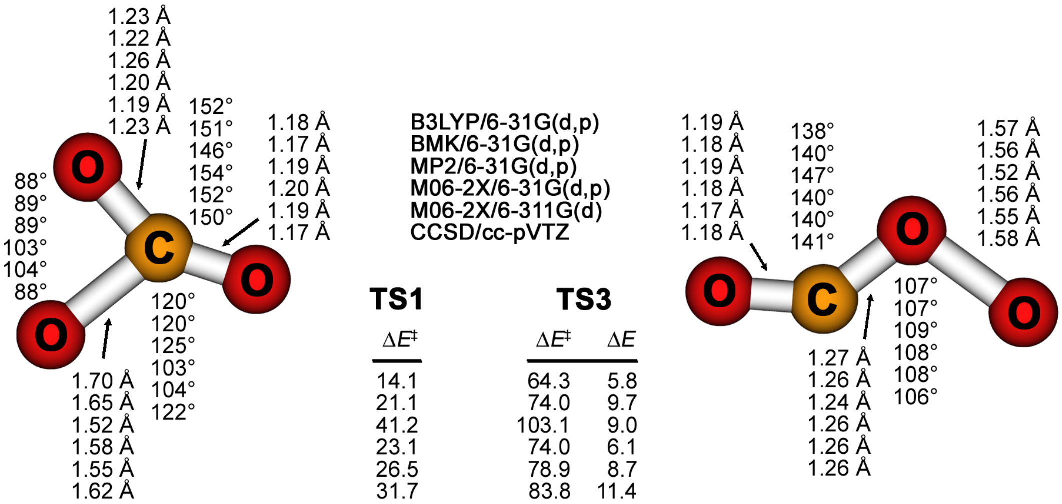

TS1	TS3	
$\Delta E^\ddagger$	$\Delta E^\ddagger$	ΔE
14.1	64.3	5.8
21.1	74.0	9.7
41.2	103.1	9.0
23.1	74.0	6.1
26.5	78.9	8.7
31.7	83.8	11.4

Figure 4.3: **Comparison of TS1 and TS3 geometries and energies at various levels of theory.** ZPE-corrected transition-state ($\Delta E^\ddagger$) and reaction (ΔE) energies are shown.

generally agrees well with that at CCSD(T), deviating by < 0.02 Å in the two shorter C–O bond lengths and by $< 3^\circ$ in all the bond angles. The longest bond length, however, is 0.06 Å longer at B3LYP than at CCSD(T). Its ZPE-corrected energy is also 7.3 kcal mol^{-1} lower. At the BMK level of theory, the TS1 geometry agrees with the CCSD(T) geometry within 0.02 Å in all the bond lengths and within 3° in all the bond angles, and with the CCSD(T) energy within 0.1 kcal mol^{-1}.

The CO_3 bound state had C_{2v} symmetry at the B3LYP and CCSD(T) levels of theory and C_s symmetry at the BMK level of theory. C–O bond lengths were larger than typical CO_2 bond lengths (1.21 Å), consistent with an overall decrease in C–O bond order upon CO_3 formation. The B3LYP geometry agreed within 0.04 Å and 1° with the CCSD(T) geometry, which had C–O bond lengths of 1.27 Å, 1.27 Å, and 1.30 Å and bond angles of 118°, 118°, and 123° (see Figure 4.2). The ZPE-corrected B3LYP energy, however, is 8.9 kcal mol^{-1} lower than that at CCSD(T). At the BMK level of theory, moderate agreement in the CCSD(T) geometry was observed; in addition to displaying lower symmetry, the C–O bond lengths calculated at BMK were different from CCSD(T) bond lengths by up to 0.07 Å, while the bond angles were different by up to 8°. The lower symmetry for CO_3 using the BMK functional may be a consequence of the large amount of Hartree-Fock exchange mixed into the functional [*Boese and Martin*, 2004], which can result in orbital symmetry-breaking [*Sherrill et al.*, 1999]. The ZPE corrected CO_3 energy at BMK is in better agreement, however, at 1.2 kcal mol^{-1} below the energy at CCSD(T). Both B3LYP and BMK theories do show a CO_3 potential well of 6.4 and 6.0 kcal mol^{-1}, respectively, in reasonable agreement with the CCSD(T) well depth of 4.8 kcal mol^{-1}.

TS2 and TS3 were associated with an oxygen-atom abstraction reaction producing O_2 + CO. They had C_s symmetry at all levels of theory. In both transition states, one C–O bond on the parent CO_2 was compressed, while the other C–O bond, which is eventually broken, was stretched (see Figure 4.2). The O–C–O bond angle was bent $\sim$40°, and the only qualitative difference between the structures was the C–O–O bond angle: The C–O–O angle bent inwards to form a ‘C’-shape in TS2, whereas it bent outwards to form a ‘S’-shape in TS3. Both B3LYP and BMK geometries agreed with the CCSD(T) geometry with a maximum discrepancy of 0.04 Å in the O–O bond length at the BMK level. The two bond angles agreed to within 2°. Resulting ZPE-corrected barrier heights showed larger discrepancies: B3LYP and BMK energies for TS2 differed from CCSD(T) values by –6.9 and +2.4 kcal mol^{-1}, respectively, while they differed from CCSD(T) values by +6.1 and –3.6 kcal mol^{-1}, respectively, in TS3. We note that BMK overpredicted the endothermicity of the $O(^3P) + CO_2 \rightarrow O_2 +$ CO reaction by ~4.5 kcal mol^{-1}; this disagreement is again probably a consequence of the large amount of Hartree-Fock exchange mixed into the BMK functional, which was included to improve the performance of the functional when predicting transition state properties.

4.3.2 Reaction dynamics calculations

QCT calculations were run on the $^3A''$ PES with both B3LYP/6-311G(d) and BMK/6-311G(d) methods. Both methods showed reasonable agreement with the geometries and energies of the stationary points calculated at CCSD(T)/aug-cc-pVTZ and were computationally affordable for direct dynamics calculations. Four hundred trajectories were run at collision energies of 1.0, 1.5, 2.5, 3.5, 4.5, 5.5, and 6.5 eV (23.0, 34.6, 57.6, 80.7, 103.7, 126.7, and 149.8 kcal mol^{-1}, respectively) using the B3LYP level of theory for a total of 2800 trajectories. This range of energies was selected because the ZPE-corrected barriers for TS1, TS2, and TS3 according to this level of theory were 17.7, 55.2, and 69.2 kcal mol^{-1} (0.77, 2.4, and 3.0 eV, respectively). In addition, four hundred BMK trajectories were run at collision energies of 1.5, 2.5, 3.5, 4.5, 5.5, and 6.5 eV for a total of 2400 trajectories. At this level of theory, the ZPE-corrected reaction thresholds were 25.0, 64.5, and 78.9 kcal mol^{-1} (1.1, 2.8, and 3.4 eV, respectively) for TS1, TS2, and TS3, respectively. The collision energy of 1.0 eV (23 kcal mol^{-1}) was not considered because it is below the threshold for both reactions 4.1 and 4.2, according to the BMK level of theory. Trajectories were integrated using a standard fifth-order predicator, sixth-order corrector integration algorithm [*Bunker*, 1970; *Press et al.*, 1992] with an integration time-step of 10.0 a.u. (0.24 fs). The energy and gradient were calculated at each point using the Q-Chem software package [*Shao et al.*, 2006], and the initial orientation and impact parameter was sampled randomly. To simulate the ZPE, an intermolecular trajectory starting from CO_2 in its equilibrium configuration was run with kinetic energy corresponding to the ZPE in each normal mode, and the atomic coordinates along this trajectory were used to sample the initial CO_2 vibrational phase randomly in subsequent trajectories.

An estimate of a reasonable value for the maximum impact parameter for reactive scattering, b_{max}, was calculated using the expression [*Levine*, 2005]:

$$b_{\mathrm{max}} = d\left(1 - \frac{E_0}{E_{\mathrm{T}}}\right)^{\frac{1}{2}} \tag{4.3}$$

where d is the distance in the transition-state structure between the center of mass of the reactant CO_2 and the colliding oxygen atom, E_0 is the transition-state energy, and E_{T} is the collision energy. Because large collision energies were of principal interest, we chose to consider the largest value for b_{max} suitable for trajectories with unlimited collision energy by setting $E_{\mathrm{T}} = \infty$ in Eq. 4.3. Reaction 4.2 had the larger of the two d values, with a value of $d \sim 4.3\ a_0$ (2.3 Å). This d value, combined with a ∼15% safety margin, suggested a $b_{\mathrm{max}} = 5.0\ a_0$ (2.6 Å); thus, the trajectories were sampled with impact parameters $0 < b < 5.0\ a_0$. Trajectories were stopped when the distance between any two atoms exceeded 12 a_0 (6.3 Å).

Energy conservation and spin contamination were checked at each time-step. Trajectories in which energy was not conserved to within 3 kcal mol^{-1} or spin contamination rose above $\langle S^2 \rangle = 2.5$ were flagged. Less than 1.3% and 10% of the B3LYP and BMK trajectories, respectively, failed to meet these acceptance criteria. Most problems were related to energy conservation, and were attributed to self-consistent field convergence to an excited electronic state. Trajectories that initially did not meet the criteria were run again using a different set of self-consistent field convergence tools, which improved the energy-conservation or spin-contamination problem in many cases. Results of the re-run trajectories were compared to their initial-run analogues, and the one that met or came closest to meeting the acceptance criteria was included in the analysis. To do otherwise would have resulted in an underestimate of the reaction cross-sections, as most of the problematic trajectories were reactive ones.

Reactive cross-sections (σ_{R}) were calculated from the QCT data using the expression:

$$\sigma_R = \frac{\pi}{p^2}\sum_{i=1}^{N_R}\frac{(2l_i + 1)l_{max}}{N_{total}} \tag{4.4}$$

where $p = (2\mu E_T)^{\frac{1}{2}}$ is the momentum of the reactant system, $l_i = b_i p$ is the angular momentum of the ith trajectory, and $l_{max} = b_{max}p$. N_R is the number of reactive trajectories in the set of N_{total} trajectories run.

The total collision cross-section, σ_{total}, was estimated using the Lennard-Jones parameters for O and CO_2 according to the expression for the total cross-section:

$$\sigma_{total} = \pi b_{total}^2 \tag{4.5}$$

where b_{total} is the radius beyond which no elastic, inelastic, or reactive scattering occurs. This radius can be estimated using the Lennard-Jones potential [*Hirschfelder et al.*, 1964]:

$$V(r) = 4\varepsilon\left[\left(\frac{r_e}{r}\right)^{12} - \left(\frac{r_e}{r}\right)^{6}\right] \tag{4.6}$$

where ε and r_e correspond to the well depth and the separation distance, respectively, at the potential minimum for an interaction between a pair of like atoms or molecules. The separation distance, r_e, is a measure of the atomic or molecular size. The values for the O-atom and for CO_2 have been estimated to be $r_e(\mathrm{O}) = 2.78$ Å and $r_e(\mathrm{CO_2}) = 3.897$ Å, respectively [*Hirschfelder et al.*, 1964; *Némethy et al.*, 1983]. Combining these radii with the usual method [*Hirschfelder and Meath*, 1967], i.e.,

$$r_e(\mathrm{O} + \mathrm{CO_2}) = \frac{1}{2}\left[r_e(\mathrm{O}) + r_e(\mathrm{CO_2})\right] \tag{4.7}$$

we calculated an intermolecular interaction distance $r_e(\mathrm{O} + \mathrm{CO_2}) = b_{total}$ of 3.34 Å and a total collision cross-section of 125.2 a_0^2, which we used to calculate the relative product yields in Section 4.4.2.4. The theoretical reactive cross-section was divided by three for the comparison with experiment because the $\mathrm{O}(^3P) + \mathrm{CO_2}$ surface is triply degenerate at large $\mathrm{O}(^3P)$–$\mathrm{CO_2}$ separation distances (see Section 4.4.2.4).

Trajectories corresponding to oxygen isotope exchange were observed at all collision

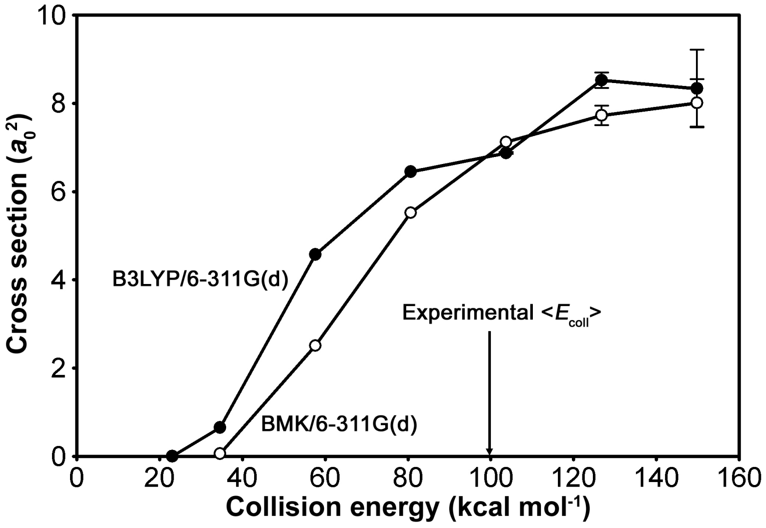

Figure 4.4: **Reactive scattering cross-sections for the O(^3P) + CO_2 isotope exchange reaction obtained from the QCT calculations.**

energies (see Table 4.2), and the resulting excitation functions were calculated from the QCT data (see Figure 4.4). These excitation functions had the same shape at the B3LYP/6-311G(d) and BMK/6-311G(d) levels of theory. The BMK excitation function was shifted to slightly higher energies compared to the B3LYP prediction, consistent with the 7.3 kcal mol^{-1} (0.32 eV) higher ZPE-corrected transition-state barrier for isotope exchange. Opacity functions for the isotope exchange reaction showed a slight decrease in reaction probability at smaller impact parameters as the collision energy increased (see Figure 4.5). $P(b)$ also appeared to reach a maximum near $b \sim 1.5 - 2\ a_0$ (1 Å).

The O_2 + CO channel appears to open at higher energies than the exchange channel (see Table 4.2), consistent with the higher ZPE-corrected transition-state barriers for the oxygen-atom abstraction reaction of 37.5 kcal mol^{-1} (1.63 eV) and 39.5 kcal mol^{-1} (1.71

Table 4.2: Number of reactive QCTs observed at different collision energies.

Theory/Basis	**Products**	**Collision energy (eV)**						
		1.0	**1.5**	**2.5**	**3.5**	**4.5**	**5.5**	**6.5**
B3LYP/6-311G(d)	O + CO_2	1	16	54	66	68	80	78
	O_2 + CO	0	0	0	0	1	4	11
BMK/6-311G(d)	O + CO_2		2	37	66	80	76	80
	O_2 + CO		0	0	0	0	5	8

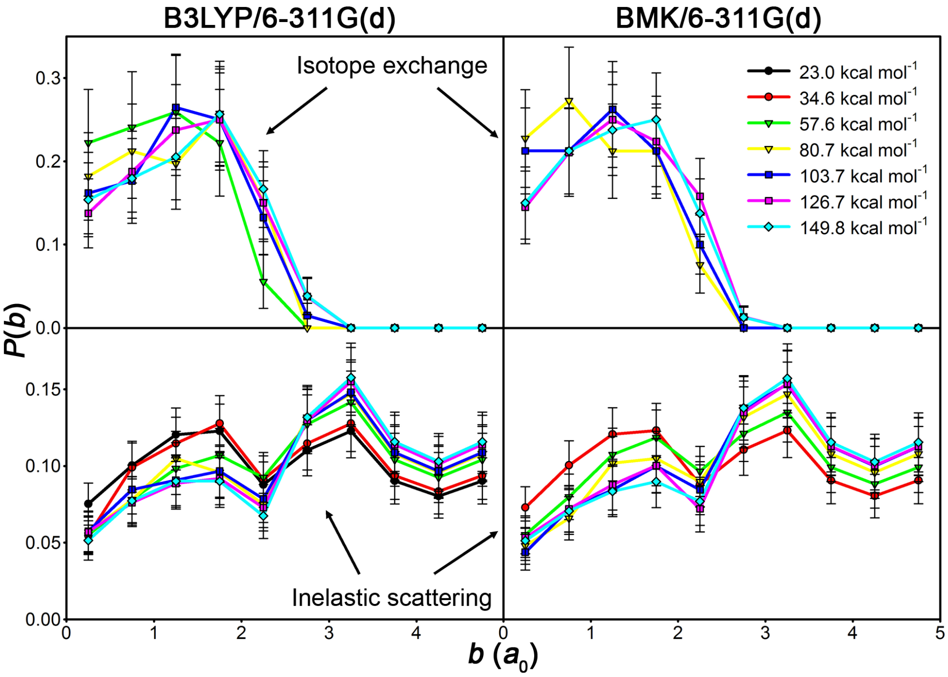

Figure 4.5: **Opacity functions for the O(^3P) + CO_2 isotope exchange reaction and for inelastic scattering of the two reagents obtained from QCT calculations at the B3LYP/6-311G(d) and BMK/6-311G(d) levels of theory.**

eV) higher than the exchange channel barrier according to the B3LYP and BMK predictions, respectively. The B3LYP threshold is slightly higher than that calculated using BMK, which is consistent with a ZPE-corrected barrier 9.3 kcal mol^{-1} (0.40 eV) larger at BMK than at B3LYP. Because only a small number of oxygen-atom abstraction reactions were observed, even at collision energies significantly in excess of the calculated reaction barrier, the amount of mechanistic insight available from the O(^3P) + $CO_2 \rightarrow O_2$ + CO reaction is limited.

A full discussion of the trajectory calculations, including the resulting product angular and translational energy distributions, can be found in Sections 4.4.2 and 4.5; they will be analyzed with the experimental data to elucidate the possible reaction mechanisms for each channel.

4.4 Experimental studies

4.4.1 Methods

Crossed-molecular-beam experiments were performed with an apparatus equipped with a hyperthermal atomic oxygen beam source at Montana State University, which was described in the preceding chapter. Briefly, a pulsed, hyperthermal beam of ~87% $^{16}O(^3P)$ and ~13% $^{16}O_2$ ($^3\Sigma_g^-$) was generated by laser-induced detonation of $^{16}O_2$ using a high-energy CO_2 TEA laser (6 – 7 J pulse^{-1}). Though initially broad in velocity distribution (6 – 9 km s^{-1}), a portion of the overall beam was velocity-selected with a chopper wheel (see Figure 3.1) at an average velocity $\langle v \rangle = 8262$ m s^{-1}. The resulting beam was crossed at a right angle with a pulsed supersonic expansion of 98% $^{12}C^{18}O_2$. The scattered products were detected with a rotatable quadrupole mass spectrometer that collected number-density distributions for each product as a function of arrival time at the ionizer, $N(t)$, at a given laboratory angle, Θ, the angle at which the product scatters with respect to the direction of the reagent oxygen beam. Time-of-flight (TOF) distributions for ^{16}O, $^{18}O^{16}O$, $^{16}O^{12}C^{18}O$, and $^{12}C^{18}O_2$ were collected over a range of laboratory angles; at each angle, the TOF distribution was integrated to give a laboratory angular distribution, $N(\Theta)$. A forward-convolution method was then used to derive c.m. translational energy $P(E_T)$ and angular $T(\theta_{\text{c.m.}})$ distributions from the laboratory $N(t)$ and $N(\Theta)$ distributions [*Lee*, 1988], where $\theta_{\text{c.m.}}$ is the angle at which a product scatters with respect to the reagent oxygen direction in the c.m. frame. The canonical Newton diagrams used in this analysis are shown in Figure 4.6.

Laboratory TOF product distributions were measured every 2° between $\Theta = 6^\circ – 54^\circ$. Scattered product TOF distributions were collected for 200 beam pulses for $m/z = 16$ ($^{16}O^+$) and 32 ($^{16}O_2{}^+$), for 1000 beam pulses for $m/z = 46$ ($^{16}O^{12}C^{18}O^+$), and for 500 beam pulses for $m/z = 48$ ($^{12}C^{18}O_2{}^+$). Scattered products at $m/z = 34$ ($^{18}O^{16}O^+$) were collected for 12000 beam pulses at $\Theta = 6^\circ$ and 10° and 6000 beam pulses at $\Theta = 14^\circ$. Dwell time for each channel at the MCP was 1 μs. At a representative laboratory angle of 10°, integrated count rates were 1.1×10^7 s^{-1} for $m/z = 16$, 1.3×10^7 s^{-1} for $m/z = 32$, 1.4×10^4 s^{-1} for $m/z = 34$ ($^{18}O^{16}O^+$), 1.8×10^5 s^{-1} for $m/z = 46$, and 4.2×10^6 s^{-1} for

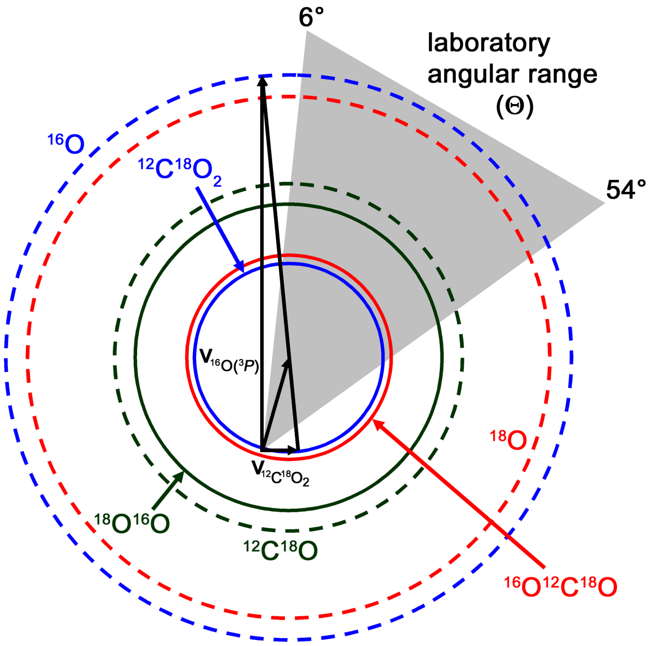

Figure 4.6: **Canonical Newton diagram for ^{16}O + ^{12}C^{18}O$_2$ collisions at E_{coll} = 98.8 kcal mol^{-1}** The ^{16}O-atom beam velocity is 8262 m s^{-1} and the ^{12}C^{18}O$_2$ beam velocity is 800 m s^{-1}. The shaded region indicates the range of laboratory angles probed. The radii of each circle represent the maximum recoil velocities of the following products of ^{16}O(^3P) + ^{12}C^{18}O$_2$ collisions: ^{12}C^{18}O$_2$ (blue solid) + ^{16}O (blue dashed), ^{16}O^{12}C^{18}O (red solid) + ^{18}O (red dashed), and ^{18}O^{16}O (green solid) + ^{12}C^{18}O (green dashed).

m/z = 48.

Three signal corrections were made before data analysis. First, we corrected for beam divergence at Θ = 6° – 16°. The divergent intensity with the ^{12}C^{18}O$_2$ beam turned off was measured by obtaining TOF distributions at m/z = 16 and 32 from Θ = 6° – 16°. These TOF distributions were then scaled and subtracted from the corresponding experimental TOF distributions at m/z = 16 and 32 that had the ^{12}C^{18}O$_2$ beam turned on. Uncertainties in the non-reactive and reactive scattering signals due to collisions of the divergent hyperthermal oxygen could not be quantified, however; they were instead considered in the analysis of the laboratory data, where collisions at crossing angles of 88°, 89°, 90°, 91°, and 92° were included during forward-convolution fitting. Adding more crossing angles did not affect the forward-convolution fits significantly. Second, we measured that the ^{12}C^{18}O$_2$ beam contained 2% ^{16}O^{12}C^{18}O using the instrument's mass spectrometer. Thus, 2% of the inelastic scattering signal (m/z = 48) at each laboratory angle (Θ = 6° – 54°) was subtracted from raw *m/z* = 46 ($^{16}O^{12}C^{18}O^+$) TOF distributions to obtain reactive-scattering-only distributions. Last, the hyperthermal O_2 beam contained 0.4% $^{18}O^{16}O$ (at natural isotopic abundances), so 0.4% of the non-reactive scattering signal (*m/z* = 32) was subtracted from the raw *m/z* = 34 ($^{18}O^{16}O^+$) TOF distributions to obtain reactive-scattering-only distributions.

4.4.2 Results

4.4.2.1 Non-reactive scattering of $^{16}O(^3P)$ and $^{12}C^{18}O_2$

The experiment mainly observed signals due to ^{16}O scattered with little deflection from its initial direction; these signals corresponded to the sum of elastic and inelastic scattering collisions of ^{16}O, which we could not resolve, so they will be referenced collectively as "scattered ^{16}O." Five representative laboratory-frame TOF distributions (*m/z* = 16), the c.m. angular and translational energy distributions and the laboratory-frame angular distribution are shown in Figure 4.7. Scattered ^{16}O had 85.6 kcal mol^{-1} total translational energy, or 87% of the available energy (see Figure 4.7B), on average. The experimental translational energy distribution was peaked at $\sim$97 kcal mol^{-1}. The c.m. angular distribution for ^{16}O was highly peaked in the forward direction with little scattered intensity for $\theta_{\text{c.m.}} > 20^\circ$; however, the velocity and angular range for ^{16}O product detection in the experiment prevented the detection of backward-scattered ^{16}O (see Newton diagram in Figure 4.6). Some dependence of the c.m. translational energy distribution on the c.m. angular distribution was observed in the ^{16}O TOF data; the forward-convolution simulations became increasingly faster than the data at larger laboratory and c.m. angles (e.g, $\Theta = 20^\circ$, 30°, and 40° in Figure 4.7A). We also note that the c.m. angular distribution for scattered ^{16}O at $\theta_{\text{c.m.}} \sim 0^\circ$ is an extrapolation because of high background from the hyperthermal oxygen source at the small laboratory angles corresponding to small c.m. angles for ^{16}O. Most of the ^{16}O probably scatters forward through high-impact-parameter collisions, but the limited constraints on the $\theta_{\text{c.m.}} \sim 0^\circ$ angular distribution (e.g., the laboratory-frame angular distribution, which only probes $\Theta = 6^\circ$) increase the uncertainty in that part of the c.m. angular distribution. This extrapolation had a small effect on the relative product yield measurements (see Section 4.4.2.4), but did not alter the results qualitatively.

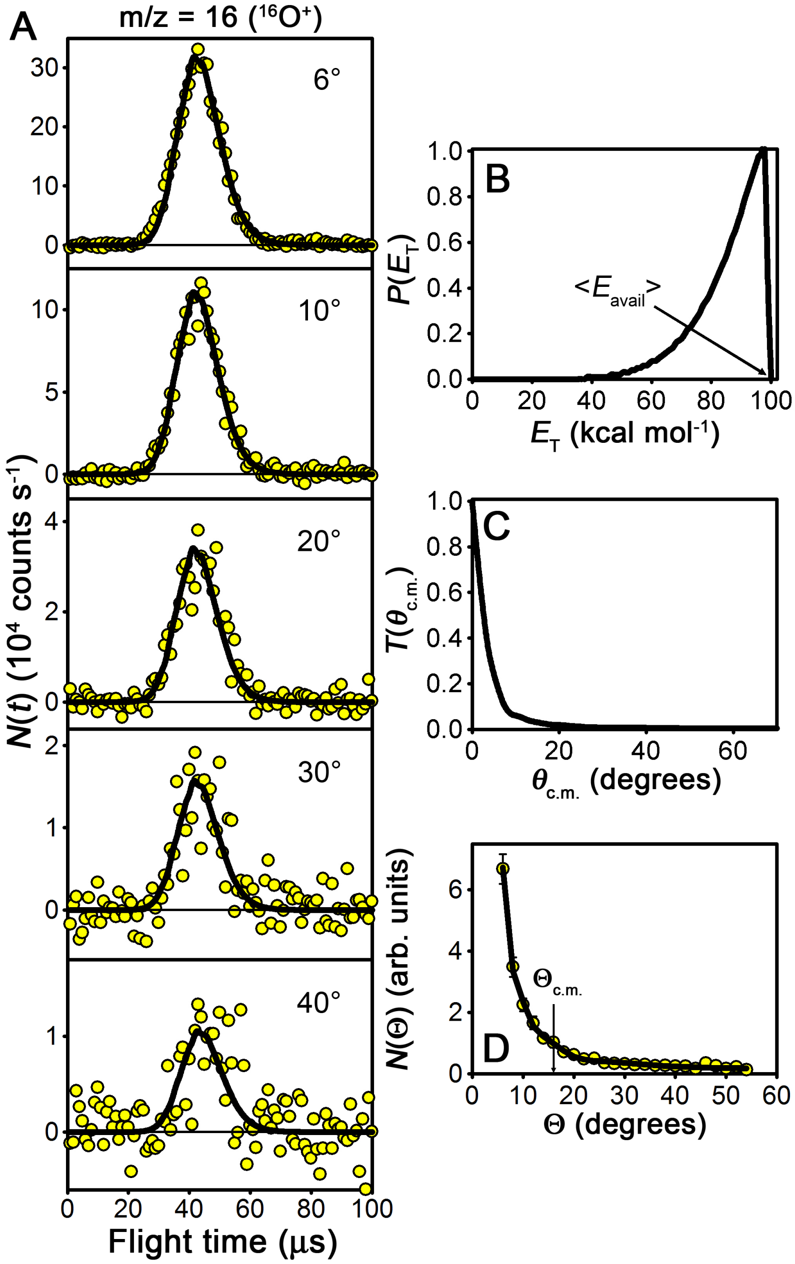

Figure 4.7: **Laboratory inelastic scattering data detected at *m/z* = 16.** (**A**) Laboratory TOF, (**B**) c.m. translational energy, and (**C**) c.m. and (**D**) laboratory angular distributions for inelastically scattered ^{16}O products from ^{16}O + $^{12}C^{18}O_2$ collisions at $\langle E_{coll} \rangle$ = 98.8 kcal mol^{-1}. The circles in (**A**) and (**D**) are experimental data, while the lines are the best-fit forward-convolution simulations of the experimental data derived from the c.m. translational energy and angular distributions shown in (**B**) and (**C**), respectively. The error bars in (**D**) represent 2σ uncertainties in the integrated experimental TOF distributions (see Appendix 4.7). These data indicate that ^{16}O is scattered mainly in the forward direction with little change in its initial direction or velocity.

The experiment mainly observed $^{12}C^{18}O_2$ scattered opposite its initial direction in the c.m. frame (see Newton diagram in Figure 4.6). Detected $^{12}C^{18}O_2$ products (m/z = 48) showed best-fit c.m. translational energy distributions that were both broader and lower in energy, on average, than that obtained for forward-scattered ^{16}O. Furthermore, a single pair of $P(E_T)$ and $T(\theta_{c.m.})$ distributions was not sufficient to describe the m/z = 48 TOF distributions. Consequently, a second pair of $P(E_T)$ and $T(\theta_{c.m.})$ distributions was included in the fit of inelastically scattered $^{12}C^{18}O_2$; five representative laboratory-frame TOF distributions, the c.m. angular and translational energy distributions, and the laboratory-frame angular distribution obtained from $^{12}C^{18}O_2$ product detection are shown in Figure 4.8, along with the c.m. velocity-flux diagram in Figure 4.9. The first $P(E_T)$ and $T(\theta_{c.m.})$ pair for inelastically scattered $^{12}C^{18}O_2$ described the scattering at $\theta_{c.m.} < 120°$. In this region, the angular distribution was peaked near $\theta_{c.m.} = 60°$, though the probability of scattered products was roughly constant for all $\theta_{c.m.} < 60°$ before decaying steadily at $\theta_{c.m.} > 60°$. The corresponding translational energy distribution was peaked at ~39 kcal mol^{-1} with an average $\langle E_T \rangle$ = 40.1 kcal mol^{-1}, or 41% the available energy. The second $P(E_T)$ and $T(\theta_{c.m.})$ pair for inelastically scattered $^{12}C^{18}O_2$ described the scattering at $60° < \theta_{c.m.} < 125°$ (corresponding to the maximum $\theta_{c.m.}$ observed in the experiment); this range overlapped, in the sideways-scattering region, with the first pair. The second $T(\theta_{c.m.})$ distribution increased rapidly from $\theta_{c.m.} = 60°$ peaked near $\theta_{c.m.} = 120°$. It decayed quickly at $\theta_{c.m.} > 120°$, although this part of the distribution is uncertain because our experiment did not probe it directly. The translational energy distribution was peaked at 65 kcal mol^{-1} with an average $\langle E_T \rangle$ = 63.8 kcal mol^{-1}, or 65% the available energy. Mechanistic implications of the additional $P(E_T)$ and $T(\theta_{c.m.})$ distributions will be addressed in Section 4.5.

While the forward-convolution laboratory fitting method produced c.m. angular and translational energy distributions that yielded good fits to the data in Figures 4.7 and 4.8, they may not be unique fits to the data because of the temporal and angular width of the incident $O(^3P)$ source beam and the low resolution and SNR in the resulting TOF distributions. Small changes to the c.m. angular and translational energy distributions still produced good fits to the data that were within the uncertainty bounds of the laboratory-frame

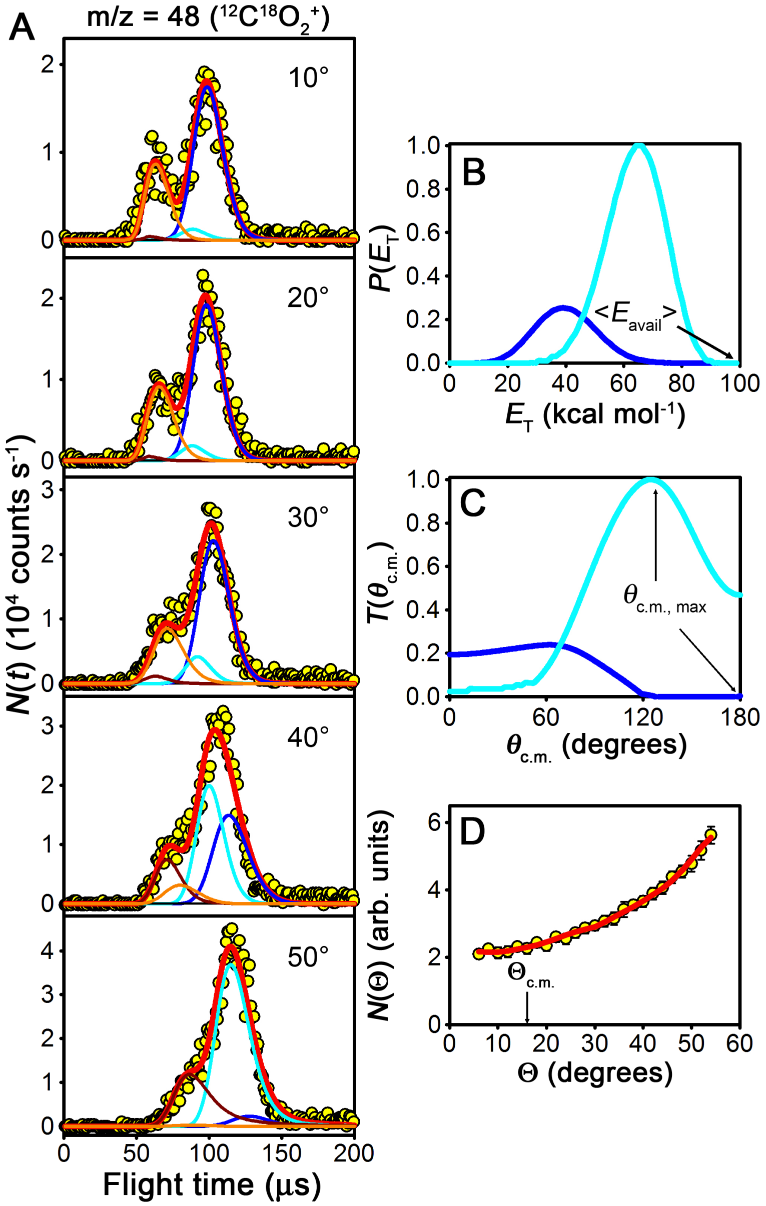

Figure 4.8: **Laboratory inelastic scattering data detected at m/z = 48.** (**A**) Laboratory TOF, (**B**) c.m. translational energy, and (**C**) c.m. and (**D**) laboratory angular distributions for inelastically scattered $^{12}C^{18}O_2$ products from $^{16}O + {}^{12}C^{18}O_2$ collisions at $\langle E_{coll} \rangle = 98.8$ kcal mol^{-1}. The circles in (**A**) and (**D**) are experimental data, while the lines (dark blue and cyan) are the best-fit forward-convolution simulations of the experimental data derived from the c.m. translational energy and angular distributions shown in (**B**) and (**C**), respectively. The error bars in (**D**) represent 2σ uncertainties in the integrated experimental TOF distributions (see Appendix 4.7). The orange and brown lines correspond to products of $^{16}O_2 + {}^{12}C^{18}O_2$ collisions, and they are discussed in Appendix 3.A. A single c.m. translational energy and angular distribution for each collision partner was insufficient to describe the TOF distributions of inelastically scattered $^{12}C^{18}O_2$, suggesting a scattering dependence on impact parameter.

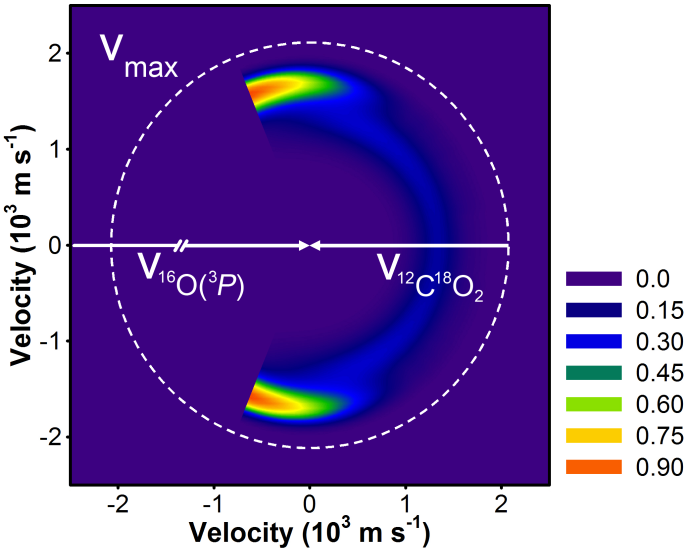

Figure 4.9: **Velocity-flux contour diagram for inelastically scattered $^{12}C^{18}O_2$ from $^{16}O(^3P)$ + $^{12}C^{18}O_2$ collisions in the center-of-mass frame.** The white arrows are the initial $^{16}O(^3P)$ and $^{12}C^{18}O_2$ velocity vectors, and the dashed white line is the maximum recoil velocity for $^{12}C^{18}O_2$ (v_{max}). Only the c.m. angles for which the experiment were sensitive are shown; inelastically scattered $^{12}C^{18}O_2$ from high-impact-parameter collisions are not shown, as their flux would be off-scale. Strong coupling of the $P(E_T)$ and $T(\theta_{c.m.})$ distributions was observed.

angular distribution (see Figures 4.7D and 4.8D), but larger, qualitative changes to the c.m. angular and translational energy distributions did not. Consequently, general statements regarding the scattering direction and degree of energy transfer in the c.m. frame can be made with some certainty.

The c.m. angular and translational energy distributions derived from the QCT calculations at E_{coll} = 4.5 eV (103.7 kcal mol^{-1}) are shown in Figure 4.10 for comparison with the experimental results for scattered ^{16}O. Center-of-mass angular and translational energy distributions for inelastic scattering obtained from the QCT calculations were in qualitative agreement with the laboratory data, although there are noticeable quantitative disagreements. The theoretical c.m. angular distribution showed fewer scattered products at $\theta_{c.m.} < 20°$ and more scattered products at $40° < \theta_{c.m.} < 90°$. In addition, the theoretical c.m. translational energy distribution had a sharper peak at high energies and a broader tail at low energies, although the average translational energies were similar ($\langle E_T \rangle$ = 85 and 86 kcal mol^{-1} for B3LYP and BMK, respectively). However, forward convolution of these dis-

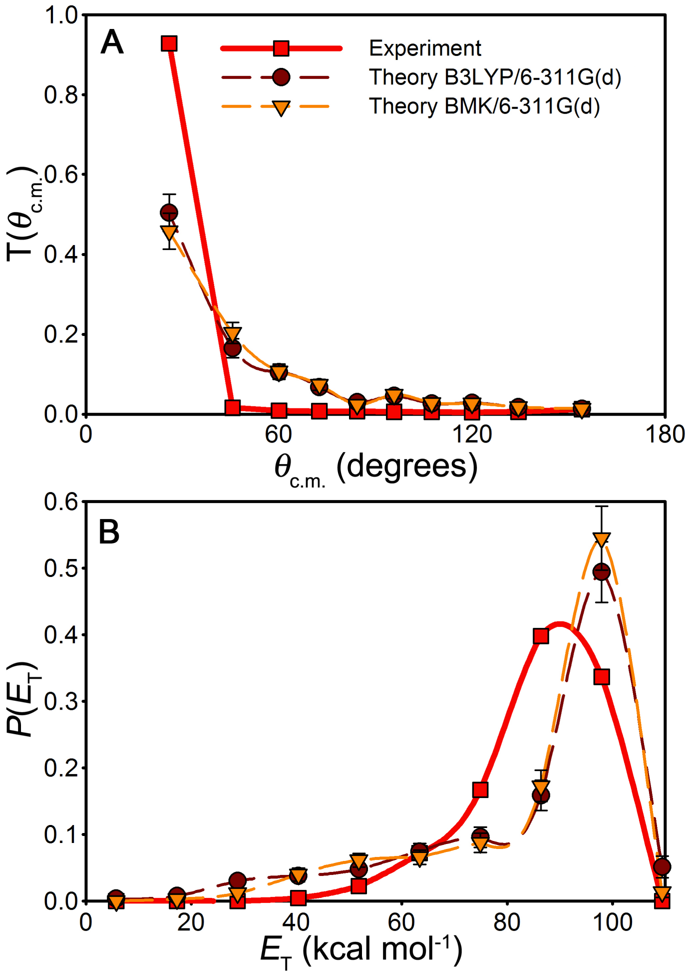

Figure 4.10: **Comparison of laboratory and theoretical c.m. (A) angular and (B) translational energy distributions for inelastic scattering of $O(^3P)$ and CO_2 at $\langle E_{coll} \rangle \approx 100$ kcal mol^{-1}.** Distributions obtained from the inelastic scattering of ^{16}O and from the QCTs are shown here. They were binned (midpoints are shown, connected by spline curves) to provide better statistics for comparison. Both B3LYP and BMK theories show fewer forward-scattered products than were observed in the experiment. Also, the theories predict a translational energy distribution that is more highly peaked at high energies and that has a longer tail at low energies.

tributions resulted in simulations of the laboratory data that underestimated the proportion of products scattered to low laboratory angles (i.e., $\Theta = 6°$, 8°, and 10°) and overestimated the low-energy tail in the TOF distributions. Some of this disagreement may be attributable to the ~14 kcal mol^{-1} width of the initial collision energy distribution, the inability of the experiment to resolve elastic- from inelastic-scattering contributions to the ^{16}O signal, and the observed coupling between the c.m. angular and translational energy distributions (see Section 4.5). Still, these laboratory results are consistent with previous studies of hyperthermal $O(^3P)$ scattering from small molecules; a forward-scattering preference and minimal energy transfer was also observed in our earlier studies of D_2, CO, and C_2H_6 collisions [*Brunsvold et al.*, 2008; *Garton et al.*, 2006, 2009].

4.4.2.2 $^{16}O(^3P) + {}^{12}C^{18}O_2 \rightarrow {}^{18}O + {}^{16}O^{12}C^{18}O$

As we reported in the preceding chapter, some of the fastest reactively scattered $^{16}O^{12}C^{18}O$ was attributed to an O-atom exchange reaction between fast-moving $^{16}O_2$ and $^{12}C^{18}O_2$ at $E_{coll} \sim 160$ kcal mol^{-1}. We describe here the results for the remaining product signal at $m/z = 46$, which we attribute to the $O(^3P) + CO_2$ isotope exchange reaction. Products of the isotope exchange reaction near 100 kcal mol^{-1} scattered mainly in the backward direction ($\theta_{c.m.} = 180°$), as implied by the five representative laboratory-frame TOF distributions, the c.m. angular and translational energy distributions, and the laboratory-frame angular distribution shown in Figure 4.11. The product c.m. velocity-flux diagram is shown in Figure 4.12. Significant forward and sideways scattering of products was also observed in addition to backward scattering; the $T(\theta_{c.m.})$ distribution indicates that products scattered to $0° < \theta_{c.m.} < 90°$ do so with nearly equal probability, and that scattered products become increasingly more probable as $\theta_{c.m.}$ approaches 180°. On average, the two products had 34.8 kcal mol^{-1} of total translational energy, or 35% of the available energy (see Figure 4.11B). The peak of the experimental translational energy distribution, $P(E_T)$, was ~30 kcal mol^{-1}. These results indicate a significant transfer of translational energy to internal degrees of freedom of the products, which is characteristic of reactions with significant barriers (e.g., ~25 kcal mol^{-1}).

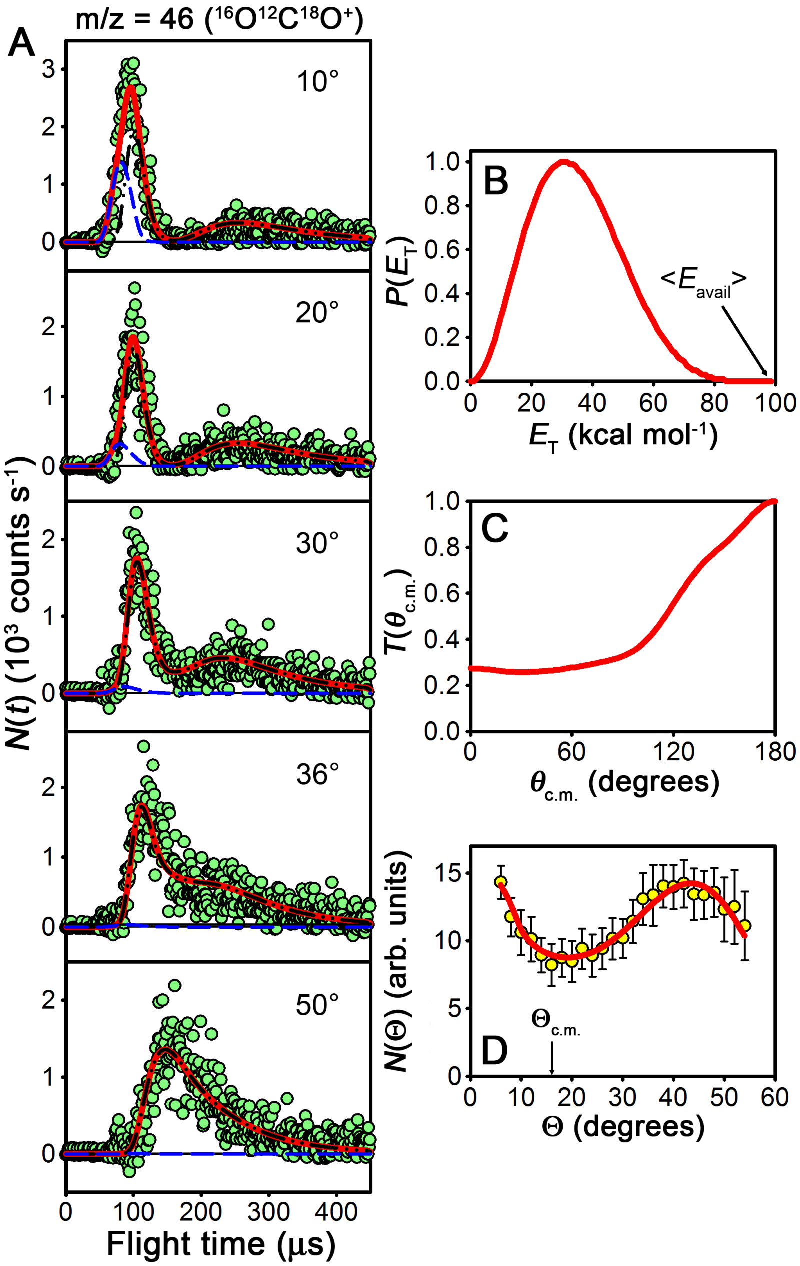

Figure 4.11: **Laboratory reactive scattering data detected at *m/z* = 46.** (**A**) Laboratory TOF, (**B**) c.m. translational energy, and (**C**) c.m. and (**D**) laboratory angular distributions for $^{16}O^{12}C^{18}O$ products of the $^{16}O(^3P) + {}^{12}C^{18}O_2 \rightarrow {}^{18}O + {}^{16}O^{12}C^{18}O$ reaction at $\langle E_{coll} \rangle = 98.8$ kcal mol^{-1}. The circles in (**A**) and (**D**) are experimental data, while the lines are the best-fit forward-convolution simulations of the experimental data derived from the c.m. translational energy and angular distributions shown in (**B**) and (**C**), respectively. In (**A**), the best-fit forward-convolution simulations of $^{16}O^{12}C^{18}O$ products from $^{16}O(^3P) + {}^{12}C^{18}O_2$ collisions (black dot-dashed lines) are shown with those from $^{16}O_2 + {}^{12}C^{18}O_2$ collisions at $\langle E_{coll} \rangle = 158.1$ kcal mol^{-1} (blue dashed lines). The error bars in (**D**) represent 2σ uncertainties in the integrated experimental TOF distributions (see Appendix 4.7).

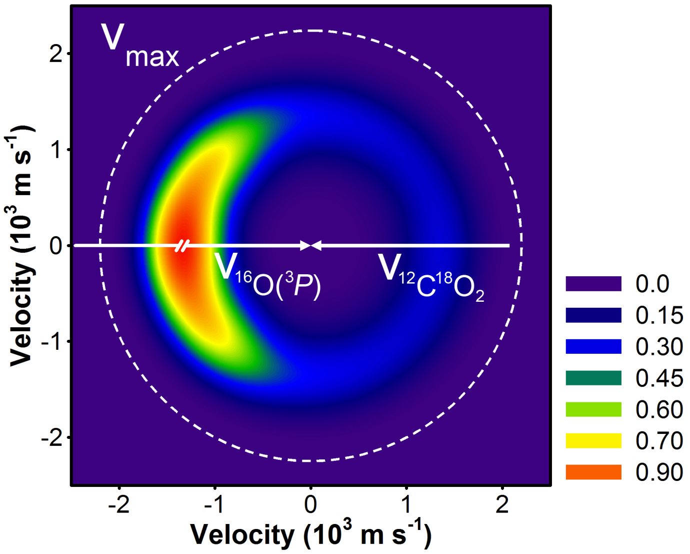

Figure 4.12: **Velocity-flux contour diagram for $^{16}O^{12}C^{18}O$ products of $^{16}O(^3P)$ + $^{12}C^{18}O_2$ collisions in the center-of-mass frame.** The white arrows are the initial $^{16}O(^3P)$ and $^{12}C^{18}O_2$ velocity vectors, and the dashed white line is the maximum recoil velocity for $^{16}O^{12}C^{18}O$ (v_{max}). $^{16}O^{12}C^{18}O$ products are scattered mainly in the same direction as the initial $^{12}C^{18}O_2$ velocity vector.

The theoretical c.m. angular and translational energy distributions derived from the QCT calculations at E_{coll} = 4.5 eV (103.7 kcal mol^{-1}) are plotted with the experimental data for comparison in Figure 4.13. In general, good agreement between experiments and the theoretical predictions was observed. The experimental best-fit c.m. angular distribution agreed nearly quantitatively for products scattered in the forward direction (small $\theta_{c.m.}$), while only qualitative agreement was found for products scattered in the backward direction (large $\theta_{c.m.}$). The preference for backward-scattered $^{16}O^{12}C^{18}O$ products suggested by the QCT calculations is also observed in the experimental data. $\langle E_T \rangle$ for the experimental $P(E_T)$ is in good agreement, within uncertainty, with those obtained from the B3LYP ($\langle E_T \rangle$ = 43 ± 15%) and BMK ($\langle E_T \rangle$ = 47 ± 16%) trajectories. Qualitative aspects of the energy transfer during reactive scattering collisions appear to be reproduced in the QCT results, namely, that the product $^{16}O^{12}C^{18}O$ has a significant amount ($\geq$ 50 kcal mol^{-1}) of internal energy, on average. The experimental peak E_T, however, is slightly less than the most probable translational energies predicted by the QCT calculations, ~40 kcal mol^{-1}.

This mild disagreement in the shape of the $P(E_T)$ distribution may arise from uncer-

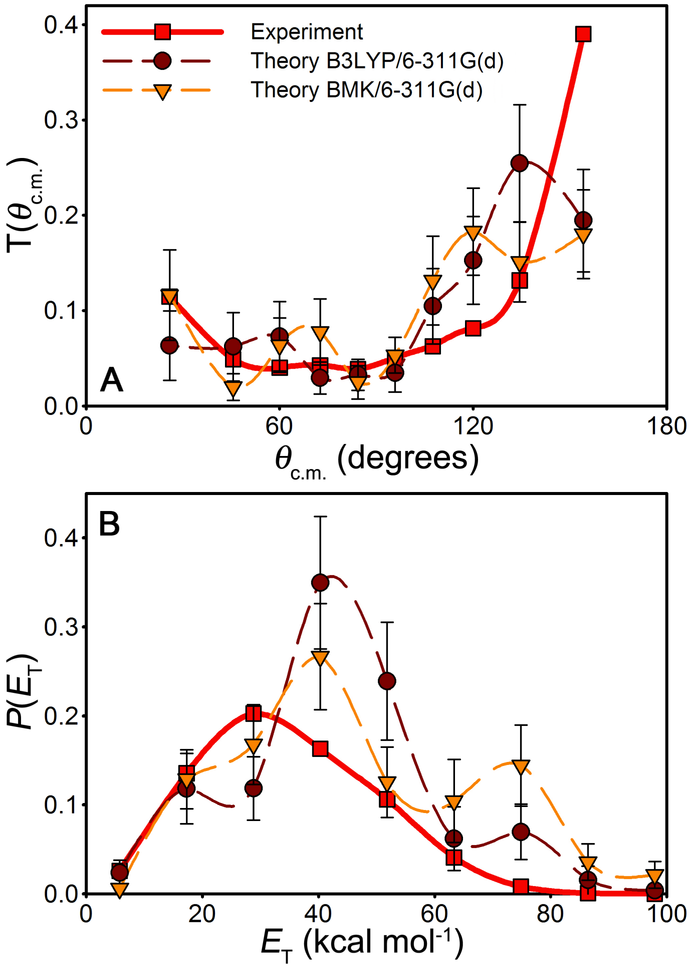

Figure 4.13: **Comparison of laboratory and theoretical c.m. (A) angular and (B) translational energy distributions for the $O(^3P)$ and CO_2 isotope exchange reaction at $\langle E_{coll} \rangle \approx$ 100 kcal mol^{-1}.** Distributions obtained from the inelastic scattering of ^{16}O and from the QCTs are shown here. They were binned (midpoints are shown, connected by spline curves) to provide better statistics for comparison. Both B3LYP and BMK theories predict fewer backward-scattered products than were observed in the experiment. Also, the theories predict a translational energy distribution that is peaked at slightly higher energies.

tainties in the experiment and in the forward-convolution analysis. First, the broad $O(^3P)$ velocity distribution in the experiment, and the resulting broad collision energy distribution, could mask any underlying structure in the $P(E_T)$ distribution if the location of the peak in the $P(E_T)$ distribution depends on collision energy. Indeed, the theoretical excitation functions indicate that the reaction cross-section is sensitive to collision energy in near E_{coll} = 100 kcal mol^{-1} (see Figure 4.4). Second, the presence of the O_2 + CO_2 isotope exchange channel, which was not resolved from the forward-scattered $^{16}O^{12}C^{18}O$ peak in the laboratory TOF, renders the higher-E_T portion of the $P(E_T)$ less certain. Constraints from the backward-scattered component of the laboratory TOF distributions were also limited due to the t^{-3} dependence of the scattered product intensity in the laboratory-to-c.m.-frame Jacobian transformation (see Eq. 3.3), which reduces the instrument's sensitivity to backward-scattered products. Consequently, the angular distribution of products near $\theta_{c.m.}$ = 180° is less certain, and the observed disagreement between experimental and theoretical c.m. angular and translational distributions could be refined with additional measurements. Last, some uncertainty in the average and peak of the product translational energy distribution in the QCT data arises from the binning process used to obtain better statistics in the distribution; the width of each E_T bin was ~11.5 kcal mol^{-1}, so disagreements in the $P(E_T)$ peak locations between theory and experiment on the order of 10 kcal mol^{-1} are not unreasonable.

4.4.2.3 $^{16}O(^3P) + {}^{12}C^{18}O_2 \rightarrow {}^{18}O^{16}O + {}^{12}C^{18}O$

Reactively scattered products at m/z = 34 were clearly resolved at Θ = 6°, barely detectable at Θ = 10°, and not detectable at Θ = 14° (see Figure 4.14). While this laboratory-frame angular dependence may imply that $^{18}O^{16}O$ products are mainly forward-scattered, we cannot rule out backward scattering because the experiment was not sensitive to it (see Newton diagram in Figure 4.6); the signal corresponding to the counterproducts at m/z = 30 ($^{12}C^{18}O^+$) could not be resolved because of high background signal from $^{12}C^{18}O_2$ fragmentation at the ionizer. We obtained a c.m. translational distribution peaked at 56 kcal mol^{-1} from the laboratory data, which indicated that $^{18}O^{16}O$ + $^{12}C^{18}O$ products had 55.0

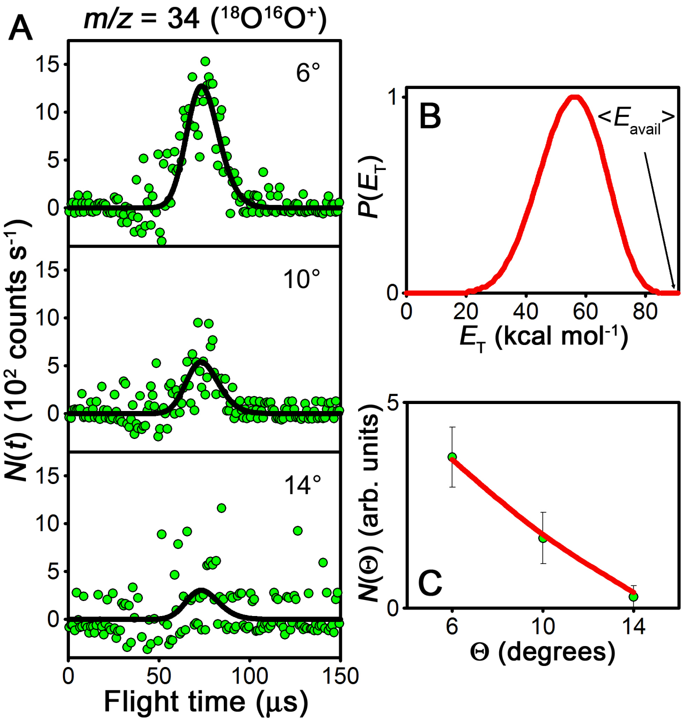

Figure 4.14: **Laboratory reactive scattering data detected at *m/z* = 34.** (**A**) Laboratory TOF, (**B**) c.m. translational energy, and (**C**) laboratory angular distributions for $^{18}O^{16}O$ products of the $^{16}O(^3P) + {}^{12}C^{18}O_2 \rightarrow {}^{18}O^{16}O + {}^{12}C^{18}O$ reaction at $\langle E_{coll} \rangle = 98.8$ kcal mol^{-1}. The circles in (**A**) and (**C**) are experimental data, while the lines are the best-fit forward-convolution simulations of the experimental data derived from the c.m. translational energy distribution shown in (**B**). Experimental sensitivity was not sufficient to obtain a full c.m. angular distribution, so a $T(\theta_{c.m.})$ distribution is not shown. The error bars in (**C**) represent 2σ uncertainties in the integrated experimental TOF distributions (see Appendix 4.7).

kcal mol^{-1} translational energy, or 61% of the available energy, on average. No products were detected at $m/z = 36$ ($^{18}O_2{}^+$), which would have corresponded to an oxygen-atom abstraction mechanism more complex than simple stripping. Qualitatively, these results are consistent with the QCT results, which predicted a lower reactive cross-section for the oxygen abstraction channel than for the isotope exchange channel.

4.4.2.4 Relative product yields

Experimental relative product yields for $^{16}O(^3P) + {}^{12}C^{18}O_2$ collisions at $\langle E_{coll} \rangle = 98.8$ kcal mol^{-1} were calculated from the integrated cross-sections for each channel, which were obtained from the forward-convolution simulations of the TOF data. Because the signal at $m/z = 46$ contained contributions from both $^{16}O(^3P) + {}^{12}C^{18}O_2$ and $^{16}O_2 + {}^{12}C^{18}O_2$ collisions,

Table 4.3: Comparison of experimental and theoretical yields for the products of $O(^3P)$ + CO_2 collisions near 100 kcal mol^{-1*}

	Non-reactive scattering	Oxygen isotope exchange
Experiment	98.4%	1.6%
B3LYP/6-311G(d)	98.2%	1.8%
BMK/6-311G(d)	98.1%	1.9%

*Uncertainty bounds in the experimental estimates are probably less than ± 0.25%, based on the uncertainties in the integrated count rates at m/z = 46. Uncertainties in the QCT-derived relative yields are less than ± 0.1%.

the forward-convolution fits for $^{16}O_2$ + $^{12}C^{18}O_2$ isotope exchange were subtracted from the laboratory TOF data before the $^{16}O(^3P)$ + $^{12}C^{18}O_2$ cross-section was calculated. Resulting integrated cross-sections were scaled by their electron-impact ionization cross-sections and fragmentation patterns for the comparison; the transmission through the quadrupole mass filter was assumed to be similar for all the small molecules examined here. Using this method, we calculated branching fractions for non-reactive scattering (98.5%), oxygen-atom abstraction (0.0004%), and oxygen isotope exchange (1.6%) based on the integrated cross-sections obtained at $m/z = 16$, 34, and 46, respectively. The oxygen-atom abstraction yield is a lower limit because only a portion of the Newton sphere was observed. The oxygen isotope exchange yield is an upper limit because we compared the integrated cross-section of $^{16}O^{12}C^{18}O$ products to the yield of scattered ^{16}O only; the strongly coupled $P(E_T)$ and $T(\theta_{c.m.})$ distributions for inelastic scattering make momentum-matching of ^{16}O and $^{12}C^{18}O_2$ products difficult.

Our experimental branching fractions for the isotope exchange reaction at $\langle E_{coll} \rangle = 98.8$ kcal mol^{-1} and those calculated from the QCT calculations at $E_{coll} = 4.5$ eV (103.7 kcal mol^{-1}) agree within 0.3%, despite a difference of 5 kcal mol^{-1} in the collision energy (see Table 4.3). This agreement could be coincidental because both the theoretical and laboratory data have significant uncertainties when defining the total cross-section, but our analysis suggests that the agreement persists in spite of these uncertainties. First, Eq. 4.4 shows that the theoretical calculation for the total cross-section depends on the square of maximum impact parameter sampled for reactive scattering (b_{max}), but examination of the theoretical opacity function for the oxygen isotope exchange reaction (Figure 4.5) indicates that no reactions occur beyond $b = 3.5\ a_0$, so the reactive cross-section should be sufficiently converged with a $b_{\max} = 5.0\ a_0$. Second, the accuracy of the laboratory integrated cross-sections depends on the accuracy of the best-fit c.m. angular and translational energy distributions, but our sensitivity study on the $\theta_{\text{c.m.}} \rightarrow 0^\circ$ extrapolation we used for scattered ^{16}O resulted in the non-reactive scattering and oxygen isotope-exchange branching fractions fluctuating ~0.5% when the scattered intensity at $\theta_{\text{c.m.}} < 4^\circ$ was varied between twice the best-fit value and zero. Third, the oxygen-atom abstraction reaction contributes to the overall reactive cross-section, but this channel had a negligible contribution to the overall product yield based on the small number of reactive trajectories observed in the QCT calculations and the small amount of $^{18}O^{16}O$ detected in the experiment. Consequently, the agreement between the theoretically derived and experimental relative product yields for the oxygen isotope exchange reaction should be robust.

The theoretical reactive cross-sections (Eq. 4.4) were divided by three for the comparison with experiment because the $O(^3P) + CO_2$ surface is triply degenerate at large $O(^3P)$–CO_2 separation distances;. All three electronic states were probed by the experiment, but only one ($^3A''$) was probed in the QCT calculations. Whether the two additional states (e.g., $^3A'$) lead to reaction under our experimental conditions is unknown, but the good agreement between theory and experiment is consistent with the other two electronic surfaces being either repulsive or unimportant for producing $^{16}O^{12}C^{18}O$ at these collision energies. If the barrier to isotope exchange on the $^3A'$ surface is close to the one the $^3A''$ surface, isotope exchange on the $^3A'$ surface could also contribute to the experimental product yield; the current theoretical product yield, therefore, should be treated as a lower limit when compared to the experimental value. Degenerate triplet states were also a concern in our study of $O(^3P) + C_2H_6$ collisions, but the laboratory relative product yields there also agreed, within uncertainty, with those derived from QCT calculations [*Garton et al.*, 2009].

4.5 Discussion

4.5.1 Theoretical studies

Our electronic structure calculations yielded some disagreements with previous work [*Bennett et al.*, 2004; *Froese and Goddard*, 1993; *Mebel et al.*, 2004; *Yang et al.*, 2005]. First, we reported a geometry and energy for TS1 structure that was significantly different from that predicted by Mebel and coworkers calculated at the CASSCF(16,13)/6-311G(d) level of theory (see Figure 4.2) [*Bennett et al.*, 2004; *Mebel et al.*, 2004]. For example, in *Mebel et al.*'s $^3A'$ TS1 structure, the longest C–O bond was 0.08 Å shorter, the shortest C–O bond was $\sim$0.02 Å longer, and the most acute bond angle was 17° smaller than in our CCSD(T)/aug-cc-pVTZ structure. Interestingly, our $^3A''$ TS1 structure shows smaller disagreements with the $^3A'$ TS1 structures calculated by Froese and Goddard at the HF/6-31G* and MP2/6-31G* levels of theory. These differences in geometries and the difference in symmetry yielded a TS1 energy 11 kcal mol^{-1} higher in *Mebel et al.*'s CCSD(T)/6-311+G(3df) calculation than in our calculation. *Mebel et al.* did note that their truncated (16,13) active space was a clear shortcoming of their study; it was chosen over the full-valence (22,16) active space due to computational limitations. Second, our calculations indicated that the lowest-energy triplet PES near TS1 had $^3A''$ symmetry, not $^3A'$ symmetry, as others had reported [*Bennett et al.*, 2004; *Froese and Goddard*, 1993; *Mebel et al.*, 2004]. We examined this discrepancy first by calculating the single-point CCSD(T)/aug-cc-pVTZ energy of Froese and Goddard's "T9" structure at both orbital symmetries. In this case, the $^3A'$ energy was $\sim$10 kcal mol^{-1} above the $^3A''$ energy. We also attempted to optimize a TS1-like $^3A'$ structure at the CCSD(T)/aug-cc-pVTZ and W4 levels of theory, but we found self-consistent field convergence problems similar to those reported by Froese and Goddard and thus could not locate any stationary points. The $^3A''$ state of CO_3 near TS1, then, appears to be lower in energy than the $^3A'$ state.

We argue that these discrepancies were caused by the differing treatment of dynamical correlation in this study and others. The electronic structure of ground singlet CO_3 displays vibronic coupling with an array of Jahn-Teller states [*Kowalczyk and Krylov*, 2007; *Liu et al.*, 2009], and the resulting energy minima required a high level of dynamical correlation to represent correctly; because of the large number of electronic states within several eV of the lowest triplet PES, vibronic coupling (and therefore dynamical correlation) is likely important here as well. Multiconfigurational self-consistent field methods like CASSCF (used by *Mebel et al.* for geometry optimizations) do not treat dynamical correlation, and this shortcoming has been implicated in the poor representation of the singlet-CO_3, NO_3, and para-benzyne radicals with these methods [*Crawford et al.*, 2001; *Eisfeld and Morokuma*, 2000; *Kowalczyk and Krylov*, 2007]. High-level dynamical correlation is included in coupled-cluster methods, which generally yield more accurate thermochemical properties for this class of problems. Furthermore, the agreement between our TS1, TS2, and CO_3 energies and those calculated using the W4 method (J. M. L. Martin, private communication) suggest that single-reference calculations with high-level treatment of dynamical correlation can describe the triplet stationary points appropriately. Multi-reference character on other regions of the PES could still be important, however, and is not ruled out by the correspondence between the CCSD(T) and W4 calculations at the stationary points.

If strong vibronic coupling on the low-lying electronic states of CO_3 is important during reactive trajectories, it could lead to a misrepresentation of the PES curvature by the B3LYP and BMK methods during the QCT calculations. *Russ et al.* [2004] noted that B3LYP underestimated the magnitude of vibronic interactions in the B–N–B and $C_3{}^+$ model systems, and attributed this tendency to the behavior of the Kohm-Sham molecular orbital Hessian near conical intersections. Because the Kohm-Sham Hessian is common to both B3LYP and BMK theories, both functionals are subject to the same tendency. Large fractions of Hartree-Fock exchange mixed into the BMK functional for improved barrier height prediction may also result in unintended symmetry-breaking on the CO_3 PES [*Sherrill et al.*, 1999], as was the case for the CO_3 minimum (see Figure 4.2). The results of these calculations are compared with the experimental results below.

4.5.2 Non-reactive scattering of $O(^3P)$ and CO_2

Non-reactive $^{16}O(^3P)$ + $^{12}C^{18}O_2$ collisions mainly scattered products with little change in the initial direction or speed, although some products scattered in directions sideways and opposite their initial direction; these products had lower average velocities. Products showing little deflection from their initial trajectories probably arise from high-impact-parameter collisions, while products that are highly deflected probably arise from low-impact-parameter collisions. These two molecular regimes were supported qualitatively by the theoretical opacity functions (see Figure 4.5), which display separate peaks at low (1.75 a_0) and high (3.25 a_0) impact parameters. While large impulsive energy transfer was observed for hyperthermal collisions of Ar and $O(^3P)$ with C_2H_6 at low impact parameters [*Brunsvold et al.*, 2004; *Garton et al.*, 2009; *Tasic et al.*, 2007], large energy transfer was also observed for "failed" reactive collisions of hyperthermal $O(^3P)$ and CO; the CO_2* complex resulting from these collisions can dissociate to yield products corresponding to isotope exchange or inelastic scattering, depending on the identity of the dissociating oxygen atom. This mechanism resulted in a low-energy tail in the translational energy distribution for inelastic scattering of $O(^3P)$ + CO [*Brunsvold et al.*, 2008].

Our analysis of inelastically scattered $^{12}C^{18}O_2$ molecules indicated that one pair of $P(E_T)$ and $T(\theta_{c.m.})$ distributions was insufficient to simulate the laboratory data accurately. This observation corresponds to a breakdown of the assumption that the c.m. angular and translational energy distributions are separable. Our use of two pairs of $P(E_T)$ and $T(\theta_{c.m.})$ distributions to fit the laboratory data is similar to previous studies where inelastic scattering of Cl + C_3H_8 and hyperthermal $O(^3P)$ + C_2H_6 were investigated [*Blank et al.*, 1998; *Garton et al.*, 2009]. In both the previous cases and in the present case, the polyatomic species had a large number of degrees of freedom into which translational energy can be transferred upon collision. Consequently, a dependence of energy transfer on the impact parameter is not unexpected; different impact parameters may preferentially excite different degrees of freedom. In the system studied here, the product translational energy decreases as $^{12}C^{18}O_2$ becomes more forward-scattered (small Θ, corresponding to low-impact-parameter collisions), implying that $^{12}C^{18}O_2$ becomes increasingly internally excited as O–CO_2 collisions become more rebound-like. The type and mechanism of internal excitation are uncertain, however, because the "failed" reaction might also contribute to the observed c.m. angular and translational energy distributions of forward-scattered $^{12}C^{18}O_2$. We note that our experimental data did not display a slow tail in the ^{16}O TOF distributions characteristic of the "failed" reaction in the $O(^3P)$ + CO system.

4.5.3 Oxygen isotope exchange, $O(^3P) + CO_2 \rightarrow O + CO_2$

Laboratory data for the isotope exchange reaction at $\langle E_{coll} \rangle$ = 98.8 kcal mol^{-1} shows a backward-scattering preference, and thus is evidence for a direct reaction mechanism. The isotopically exchanged products also had relatively low translational energy ($\langle E_T \rangle$ = 35% E_{avail}). These two observations suggest that the reaction involves a short-lived $CO_3{}^*$ intermediate and/or occurs at low impact parameters where the transfer of energy to internal degrees of freedom of the products is efficient. With 74 kcal mol^{-1} excess energy, the $O(^3P)$–CO_2 collision need not be head-on to have enough energy to surmount the TS1 activation barrier. The long C–O bond length (1.6 Å) and mild O–C–O bending angle (150° vs. 180° for CO_2) in TS1 also suggests that the entrance and exit barriers are neither particularly early nor late. Hence, the $CO_3{}^*$ complex could exist for several vibrational periods. Efficient transfer of energy into vibrational modes of the $CO_3{}^*$ intermediate would be required for an isotope exchange event to occur because inefficient coupling of that energy would increase the probability of redissociating the incident oxygen atom, resulting in an inelastic collision.

A direct isotope exchange mechanism through a short-lived CO_3 complex is qualitatively in agreement with our QCT calculations (see Figure 4.15). For $O(^3P)$ + CO_2 collisions

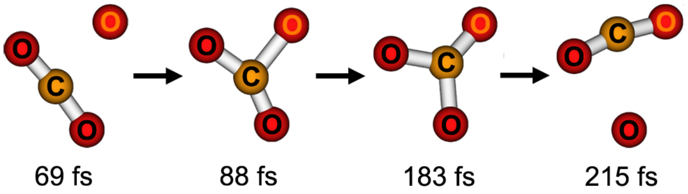

Figure 4.15: **Snapshots of a quasiclassical trajectory for $O(^3P)$ + CO_2 isotope exchange through a short-lived $CO_3{}^*$ complex at 1.5 eV (34.6 kcal mol^{-1}) collision energy.** The incident oxygen atom is highlighted for clarity.

resulting in oxygen isotope exchange, a CO_3^* complex forms when the incoming oxygen atom interacts with the carbon atom on CO_2 (see also the opacity functions in Figure 4.5). In some cases, the CO_3^* complex existed for less than one vibrational period (the reaction is nearly direct) while in others it existed for many vibrational periods. After some time (typically leq 200 fs), one of the oxygen atoms initially part of the CO_2 detaches to leave behind a new CO_2 molecule. Head-on collisions at higher collision energies tended to form complexes existing for shorter times than those formed similarly at lower energies. Higher energies also tended to form CO_3^* complexes that tumbled $\geq 360^\circ$ in the plane of the reaction. In all cases, however, the CO_3^* complex lasted less than a picosecond.

These data support an isotope exchange reaction mechanism that begins with an interaction between $O(^3P)$ and the carbon atom of CO_2 to form a short-lived CO_3^* reaction complex. The identity of the dissociating oxygen atom determines the reaction's classification. If the dissociating oxygen atom is one originally on CO_2, then the trajectory is reactive; if it is the incident oxygen atom, then the trajectory is inelastic. The lifetime of the CO_3 reaction complex determines the c.m. angular and translational energy distributions of product CO_2. Longer-lived CO_3 complexes should yield smaller average translational energies because they will have more time to redistribute the initial translational energy to internal degrees of freedom.

This mechanism for the $O(^3P) + CO_2$ isotope exchange reaction is different from that observed by *Perri et al.* for the $O(^1D) + CO_2 \rightarrow O(^3P) + CO_2$ isotope exchange reaction at $E_{\text{coll}} = 4.2$ and 7.7 kcal mol^{-1}, which samples part of the same PES [*Perri et al.*, 2003, 2004]. In those molecular-beam experiments, the reactively scattered CO_2 products had an isotropic (forward-backward symmetric) angular distribution and $\sim$50% of the available energy in translation; these results were evidence for a CO_3^* intermediate complex that lasted for at least several rotational periods (> 1 ps). These dynamics are not inconsistent with our $O(^3P) + CO_2$ results, however, because the two studies may sample different parts of the $^3A''$ and/or $^3A'$ PESs.

$O(^3P) + CO_2$ collisions on the $^3A'$ surface could, in principle, cross onto the $^1A'$ surface to yield reactively scattered $O(^1D) + CO_2$ products. One possible triplet-singlet crossing mechanism could be through spin-orbit coupled radiationless transitions, i.e., the reverse of what *Mebel et al.* had suggested for the O(^1D) + CO_2 reaction, because the spin-orbit coupling terms and Franck-Condon factors are favorable [*Mebel et al.*, 2004]. Thus, we evaluated the general possibility of intersystem crossing (ISC) during our experiments by performing forward-convolution fits of the laboratory data that included the ~45 kcal mol^{-1} endothermicity of O(^1D) vs. O(^3P). Satisfactory fits of the laboratory TOF and angular distributions were obtained (see Figure 4.16); the peak and average of the $P(E_T)$ distribution were 34 and 30.7 kcal mol^{-1} (63% and 58% E_{avail}), respectively. Consequently, ISC cannot be explicitly ruled out by the experimental data. The diabatic radiationless transition probability, however, decreases exponentially as a function of velocity [*Landau*, 1932], and no evidence for ISC has been observed during our previous dynamics studies at hyperthermal velocities [*Brunsvold et al.*, 2007]. The qualitative agreement between the experimental and QCT-derived dynamics on the lowest triplet PES is consistent with the oxygen isotope exchange reaction exiting on a triplet surface, although more dynamics studies will be necessary to test this hypothesis.

4.5.4 Oxygen-atom abstraction, O(^3P) + $CO_2 \rightarrow O_2$ + CO

Our laboratory observation of the oxygen abstraction reaction in the forward direction with a moderate amount of energy transfer (~50%) could arise from early-barrier stripping-type mechanisms through TS2 or TS3. Hammond's postulate states that for endothermic reactions, the transition state should be late and product-like. However, the small endothermicity relative to the barrier height (see Figure 4.1 and Table 4.1) for oxygen-atom abstraction suggests that TS2 and TS3 should be more reactant-like. Indeed, the bond lengths of CO and O_2 are significantly longer in TS2 and TS3 than at equilibrium for the isolated molecules, which are 1.14 and 1.21 Å, respectively, at CCSD(T)/aug-cc-pVTZ.

Theoretical trajectories yielding O_2 + CO products occurred generally in one of two ways: through a stripping-type mechanism and through a $CO_3{}^*$ complex. In the stripping-type mechanism (see Figure 4.17A), the incoming oxygen atom interacts principally with one of the oxygen atoms on CO_2 to form TS3 directly. The C–O bond then breaks, releas-

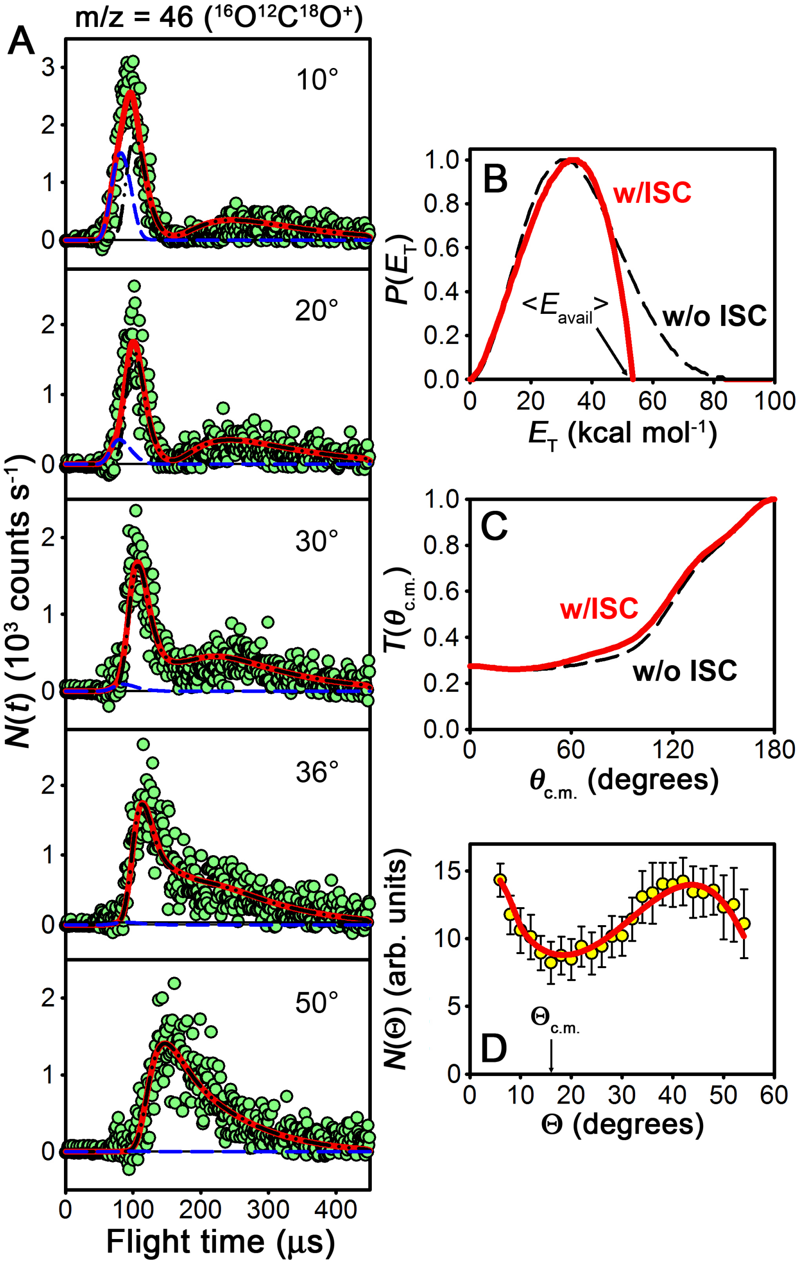

Figure 4.16: **Laboratory reactive scattering data detected at m/z = 46, fit assuming an ISC mechanism.** (**A**) Laboratory TOF, (**B**) c.m. translational energy, and (**C**) c.m. and (**D**) laboratory angular distributions for $^{16}O^{12}C^{18}O$ products of the $^{16}O(^3P) + {}^{12}C^{18}O_2 \rightarrow {}^{18}O^{16}O(^1D) + {}^{12}C^{18}O$ reaction at $\langle E_{coll} \rangle = 98.8$ kcal mol^{-1}. The circles in (**A**) and (**D**) are experimental data, while the lines are the best-fit forward-convolution simulations of the experimental data derived from the c.m. translational energy and angular distributions shown in (**B**) and (**C**), respectively. In (**A**), the best-fit forward-convolution simulations of $^{16}O^{12}C^{18}O$ products from $^{16}O(^3P) + {}^{12}C^{18}O_2$ collisions (black dot-dashed lines) are shown with those from $^{16}O_2 + {}^{12}C^{18}O_2$ collisions at $\langle E_{coll} \rangle = 158.1$ kcal mol^{-1} (blue dashed lines). The error bars in (**D**) represent 2σ uncertainties in the integrated experimental TOF distributions (see Appendix 4.7).

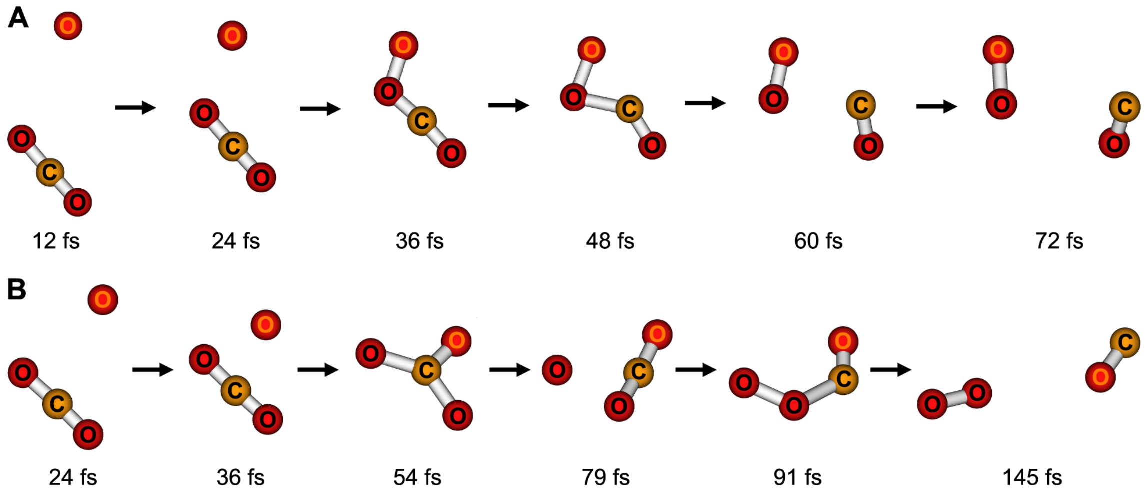

Figure 4.17: **Snapshots of quasiclassical trajectories for the $O(^3P) + CO_2 \rightarrow O_2 + CO$ reaction.** (**A**) A stripping-type mechanism through TS3 at 6.5 eV (149.8 kcal mol^{-1}) collision energy calculated at the B3LYP/6-311G(d) level of theory. (**B**) A CO_3 reaction-complex mechanism through TS2 at 5.5 eV (126.7 kcal mol^{-1}) collision energy calculated at the BMK/6-311G(d) level of theory. The incident oxygen atoms are highlighted for clarity.

ing O_2 + CO products. Of all the QCTs run, only two of these stripping-type trajectories were observed, and they occurred at E_{coll} = 6.5 eV (149.8 kcal mol^{-1}) using B3LYP/6-311G(d). The remaining 27 O_2 + CO-producing trajectories proceeded through a $CO_3{}^*$-complex mechanism (see Figure 4.17B). In that mechanism, the incoming oxygen atom interacts first with the carbon atom of CO_2 to form a short-lived $CO_3{}^*$ complex, similar to that observed in the isotope-exchange trajectories. This complex rarely survived more than one vibrational period. An oxygen atom is then released and then interacts with a CO_2-bound oxygen atom as the CO_2 rotates. Last, an O–O bond forms as the adjacent C–O bond breaks to form O_2 + CO products.

A key difference between the two O_2 + CO-producing mechanisms is that the $CO_3{}^*$-complex mechanism requires a slow recoil of the oxygen atom that dissociated initially. Following complex formation in a high-energy collision, the nascent CO_2 will have sufficient internal energy (~70 kcal mol^{-1}) to form the O_2 + CO products only if the O atom dissociates with low translational energy. When the O atom escapes the $CO_3{}^*$ complex with high translational energy, the nascent CO_2 rotates too slowly for any further reaction to take place (in these cases, the trajectory results in either inelastic scattering or isotope exchange). With so much excess energy, however, the reaction need not take the lowest energy path [*Zhang et al.*, 2008]; the slow recoiling oxygen atom in the CO_3^*-complex mechanism resembles the "roaming' H-atom and methyl group in formaldehyde [*Townsend et al.*, 2004] and acetaldehyde [*Houston and Kable,* 2006] photodissociation, respectively.

We note that the stripping-type mechanism would have produced $^{18}O^{16}O$ molecules in the experiment exclusively, whereas the CO_3^*-complex mechanism can produce $^{18}O_2$ in addition to $^{18}O^{16}O$. Our laboratory observation of $m/z = 34$ products is consistent with both oxygen abstraction mechanisms, but the lack of signal due to $m/z = 36$ products in the forward direction (where there was negligible background) is evidence against the CO_3^*-complex mechanism. The CO_3^*-complex mechanism, however, comprised 27 of the 29 oxygen-atom abstraction trajectories obtained from the QCT calculations, and only one of those trajectories would have produced $m/z = 34$ products. The two remaining trajectories proceeded through the stripping mechanism. This preference for the CO_3^*-complex mechanism observed in the QCT calculations may be a consequence of the $\sim$50 kcal mol^{-1} lower barrier for CO_3 formation and the $\sim$13 kcal mol^{-1} lower energy of TS2, both relative to the energy of TS3. Additional experimental and theoretical studies with a higher SNR, perhaps at higher collision energies, will be required to elucidate the mechanisms of this reaction.

4.6 Conclusions

We have investigated the dynamics of $O(^3P) + CO_2$ collisions at hyperthermal collision energies. Non-reactive scattering was dominated by high-impact-parameter collisions, which did not perturb the initial velocity of the reactants significantly. Lower impact parameters resulted in increased translational-to-internal energy transfer. Both the oxygen isotope-exchange and the atom-abstraction reaction channels were observed directly by our crossed-molecular-beam apparatus. The oxygen isotope exchange reaction displayed an anisotropic angular distribution with a large amount of translational-to-internal energy transfer, suggesting that the reaction occurs at low impact parameters through a short-lived intermediate CO_3^* complex. The mechanisms for both non-reactive scattering and oxygen isotope exchange were supported qualitatively, but not quantitatively, by the QCT calculations on the $^3A''$ surface.

Nonadiabaticity during inelastic and reactive trajectories cannot be ruled out and its effects should be investigated; both inelastic and reactive trajectories may be sensitive to the coupling between the lowest triplet ($^3A''$) PES and nearby (e.g., $^3A'$) electronic surfaces. With $\sim$100 kcal mol^{-1} collision energy, the experiment may probe regions of the PES far from the TS1, TS2, TS3, and CO_3 structures; the presence of several other surfaces (both triplet and singlet) within this energy range [*Kowalczyk and Krylov*, 2007; *Liu et al.*, 2009], the possibility of vibronic effects due to Jahn-Teller-like distortion, and the failure of density-functional methods to capture the dynamics quantitatively all suggest that a higher-level treatment of the PES would be desirable. While the transition states and stationary points on the lowest triplet PES may be described well with density-functional calculations, this may not be the case in other regions of the PES where vibronic interactions can affect its curvature. A more complete, high-level description of the PES, along with more dynamics experiments, will be required to describe the dynamics of isotope exchange on the lowest triplet PES quantitatively.

4.7 Acknowledgements

We thank Ned F. Lindholm for experimental assistance. This work was supported by the Missile Defense Agency under cooperative agreement HQ0006-05-2-0001. L. Y. Y. was supported by the Davidow Fund, and G. C. S. was supported by the Air Force Office of Scientific Research grant FA955D-07-1-0095.

Appendices

4.A Differential scattering cross-sections from 1.0 – 6.5 eV

Theoretical center-of-mass differential scattering cross-sections for the oxygen isotope exchange reaction (Figure 4.18) showed a preference for backward scattering at all collision energies. The incident oxygen atom, attached to the product CO_2 molecule, appeared to prefer scattering in a direction opposite its initial direction. As the collision energy increased, however, the angular distribution of products showed little qualitative change: Reactively scattered products showed a slight preference for backward scattering up to E_{coll} = 6.5 eV (149.8 kcal mol^{-1}), the highest collision energy considered in this study.

The theoretical c.m. product translational energy distributions showed significant ($\geq$ 50%) transfer of the available energy into internal degrees of freedom of the products at all collision energies = 2.5 eV (57.6 kcal mol^{-1}). The QCT data below $E_{\mathrm{coll}} \geq 2.5$ eV did not contain statistically significant number of reactive trajectories, i.e., > 30, so they were not included in this analysis. $P(E_{\mathrm{T}})$ distributions became broader as the collision energy increased, though the proportion of energy remaining translation was similar at all collision energies. A bimodal distribution of translational energies may exist in the products of BMK trajectories run at 2.5, 3.5, and 4.5 eV collision energy (57.6, 80.7, and 103.7 kcal mol^{-1}, respectively); for instance, separate peaks were observed at $\sim$50% and $\sim$80% of the available energy for the 2.5-eV trajectories, although there is considerable uncertainty in the theoretical translational energy distribution (see Figure 4.18). Additional QCT calculations will be required before structure in the product translational energy distributions can be determined conclusively.

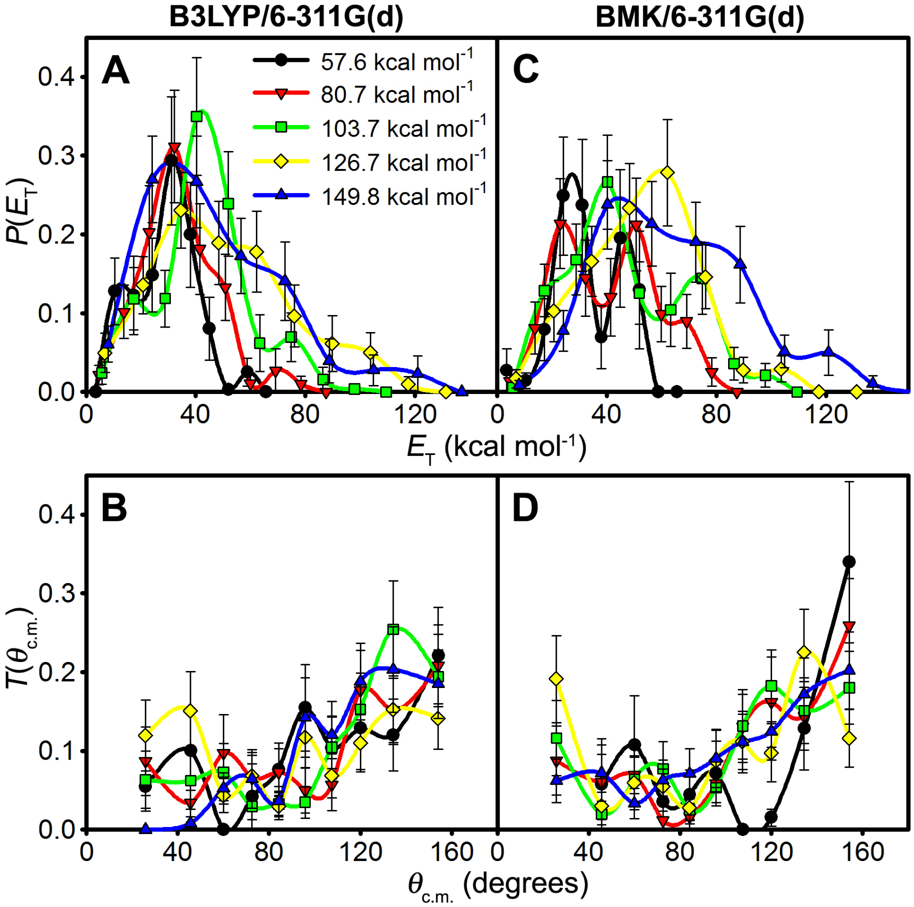

Figure 4.18: **Center-of-mass angular and translational energy distributions for the O(^3P) + CO_2 isotope exchange reaction derived from QCT calculations at the (A and B) B3LYP/6-311G(d) and (C and D) BMK/6-311G(d) levels of theory.** Distributions with more than 30 reactive trajectories are shown. At both levels of theory and all collision energies shown, reactive scattering shows a preference for backward scattering ($\theta_{\text{c.m.}} > 90°$) with a moderate ($\geq 50\%$) transfer of translational energy to internal degrees of freedom of the products.

4.B Estimating uncertainty in the laboratory angular distributions

For this analysis we treat the TOF distribution at a given laboratory angle Θ as a type of Monte Carlo integration of the 'true' TOF distribution, and we estimate the variance in the integrated area accordingly. Under this approximation, the integrated area, $I(\Theta)$, is equivalent to the area of a rectangle with a width equal to the total time range, t_{total}, and height equal to the average number density over that time range, $\langle N(t)\rangle_{\text{total}}$. More formally, this relation can be written as a discrete sum over the channels on the MCP, each of which corresponded to a 1 μs dwell time:

$$I(\Theta) = \sum_{i=1}^{t_{\text{total}}} N(t_i) = t_{\text{total}}[\frac{1}{t_{\text{total}}}\sum_{i=1}^{t_{\text{total}}} N(t_i)] = t_{\text{total}}\langle N(t)\rangle_{\text{total}} \tag{4.8}$$

The variance of $I(\Theta)$, however, must be evaluated as a function of time because the number density at a given arrival time at the detector, $N(t)$, varied with flight time in each TOF distribution. Consequently, the TOF distribution was further divided into a set of bins for which the variance was calculated and summed over the total TOF distribution using the following relation:

$$\sigma^2_{N(t)_{\text{bin}}} = \frac{1}{t_{\text{bin}}}\sum_{i}^{f}[t_{\text{bin}}N(t_i)]^2 - [t_{\text{bin}}\langle N(t)\rangle_{\text{bin}}]^2 \tag{4.9}$$

$$\sigma^2_{I(\Theta)} = \sum_{\text{bins}} \sigma^2_{N(t)_{\text{bin}}} \tag{4.10}$$

where i and f represent the first and last members of each data bin. The standard deviation, $\sigma_{I(\Theta)}$, was calculated by taking the square root of the variance. We note some degree of sensitivity in the calculated $\sigma_{I(\Theta)}$ values on t_{bin} because the $N(t)$ distributions show significant structure; consequently, we have reported conservative estimates of $\sigma_{I(\Theta)}$ using the minimum bin size of $t_{\text{bin}} = 3$ μs, or 3 data points per $\sigma^2_{N(t)_{\text{bin}}}$ calculation.